Doctoral Thesis

Study on GNSS Precise Positioning for Centimeter Augmentation and Millimeter Displacement Detection

March 2022

Doctoral Program in Advanced Electrical,
Electronic and Computer Systems
Graduate School of Science and Engineering
Ritsumeikan University

ASARI Koki

Intentional blank

Doctoral Thesis Reviewed
by Ritsumeikan University

Study on GNSS Precise Positioning for Centimeter Augmentation and Millimeter Displacement Detection
(センチメータ級測位補強及びミリメータ級変位検出に向けた GNSS 高精度測位に関する研究)

March 2022

2022 年 3 月

Doctoral Program in Advanced Electrical, Electronic and Computer Systems
Graduate School of Science and Engineering
Ritsumeikan University
立命館大学大学院理工学研究科
電子システム専攻博士課程後期課程

ASARI Koki
浅里 幸起

Supervisor: Professor KUBO Yukihiro
研究指導教員： 久保 幸弘 教授

Intentional blank

Acknowledgements

The author would like to express his sincere gratitude to Professor Yukihiro Kubo of Ritsumeikan University for his supervisions, suggestion and continuous warm encouragement in the preparation of this thesis.

The author would like to acknowledge his guidance and encouragement of Professor Yoshitaka Kawabata of Ritsumeikan University.

The author would also like to acknowledge his guidance and encouragement of Associate Professor Yohei Fukumizu of Ritsumeikan University.

The author would like to express his sincere gratitude to Professor Emeritus Sueo Sugimoto of Ritsumeikan University for his supervisions, suggestion and continuous warm encouragement in the preparation of this thesis.

Intentional blank

Abstract

In this thesis, novel high-accuracy positioning methods of Global Navigation Satellite System (GNSS) are proposed for centimeter augmentation and millimeter displacement detection, and its accuracy and convergence performances are validated.

The author has been developing a prototype centimeter-level augmentation service, which was adopted from the Quasi-Zenith Satellite System (QZSS) of Japan's Cabinet Office. In the proposed mathematical structure of the GNSS high-accuracy positioning augmentation system, accuracy and convergence time of the GNSS were improved by using the characteristics of 5G mobile communication networks. Compared with QZSS specifications, the horizontal root mean square improved from 3 [cm] to approximately 1 [cm], and the convergence time decreased from 60 [s] to approximately 3 [s]. These improvements can contribute to safety and mobility performances of automated navigation.

novel algorithms were also proposed for achieving millimeter displacement detection. Orthogonal functions are used in the proposed algorithms to retrieve measurement data from noise and detect the occurrence time of displacement, and the performances of the proposed method was validated. This method can reduce the displacement measurement time from the current 24 [h] to approximately 1 [h] in quasi-real time to promptly warn of impending landslide disasters. Thus, the proposed method can save many lives and considerable property.

A brief introduction is presented in Chapter 1. In Chapter 2, the structure and mechanisms of the developed centimeter augmentation system and its algorithms have been presented. This method is adopted to 3rd-Generation Partnership Project (3GPP) of mobile communication standards and can become the foundational technology of automated mobility and smart societies in the future. Chapter 3 describes the performance validation of the proposed high-accuracy positioning system though experiments using real data.

In Chapters 4 and Chapter 5, the author applied the high-accuracy GNSS positioning technology to millimeter displacement detection retrieved information of a fine displacement from observation with noise. Thus, the results revealed that novel the algorithm can be used prevent landslide disasters and structure collapses.

Thus, a realtime centimeter augmentation and semi-realtime millimeter displacement detection method with high-accuracy and short observation span can be obtained proposed by using GNSS systems and the proposed method. The proposed method can be a fundamental technology that can enable automated navigation and high-accuracy positioning, safe and manageable spatial migration and disaster management, and improvement of the quality of life.

Contents

Tables

Figures

1 INTRODUCTION

The author of the present dissertation has been developing Global Navigation Satellite System (GNSS) centimeter augmentation system and its applications [1]. The results of his development have been adopted from Japanese national GNSS system; Quasi-Zenith Satellite System (QZSS) Centimeter Level Augmentation Service (CLAS), International Organization for Standardization (ISO) 18197:2015, ISO/DIS 24246, and 3rd Generation Partnership Project of mobile communication system (3GPP) Release 16 for the precise point positioning by using smartphones and next generation internet of things (IoT). These heritages are globally leading the automated transportation of pedestrians, vehicles, maritime, aviation, and space in the 21st century.

In the initial two decades of this century, several countries provide their constellations of GNSS such as U.S. Global Positioning System (GPS) [2], Japanese QZSS [3], Russian GLONASS [4], European Galileo [5], Chinese BeiDou navigation satellite systems (BDS) [6], Indian NavIC [7], Satellite Based Augmentation Systems (SBASs) mainly for civil aviation, and they have been utilized as an international public service. GNSS positioning applications have been expanding in each region across the world.

In the purpose to maximize the capability of these GNSS constellations, the respective regions have deployed additional GNSS positioning augmentation systems using continuously operating reference station (CORS) networks. These facilities generate different types of corrections to mitigate atmospheric propagation errors and satellite errors, as well as provide integrity information. The application of these augmentation functions helps to achieve higher performance for GNSS positioning.

Along with the development of the GNSS constellations, GNSS reference stations have been established across populous and economic areas of the world. Industrialized countries have adopted precise positioning thanks to this integrated GNSS infrastructure in global, regional, and

national areas. Positioning users in other parts of the world require similar GNSS infrastructure.

This thesis addresses two development results of high-accuracy positioning using GNSS. One is realtime positioning augmentation for precise navigation with centimeter accuracy. Another is semi-realtime displacement detection with millimeter accuracy.

In Chapter 2 and Chapter 3, the author addresses centimeter augmentation for realtime positioning and navigation using the characteristics of 5th generation (5G) mobile communication services. GNSS precise positioning is said to be the first application of the 5G services. It brings lower latency and large capacity for data transmission. The author has designed a new GNSS PPP-RTK assistance system using these 5G excellences. PPP-RTK is a method of Precise Point Positioning (PPP) based on Real-Time Kinematic (RTK) networks. In the comparison to the existing system, this design made the horizontal accuracy from 3 [cm] to approximately 1 [cm] and made the convergence time from 60 [s] to approximately 3 [s]. These are the highest performances as the unidirectional assistance of real-time GNSS positioning for mass-market applications, that should be implemented into the smart society which we have been competitively building today.

In Chapter 4 and Chapter 5, the author addresses millimeter displacement detection in semi-realtime. It equips mathematical algorithms to measure a destructive displacement buried in noise using GNSS precise positioning and the orthogonal function expansion of its positioning result. In reality, there are 525 thousand places in danger of landslide in Japan. The algorithms must retrieve a millimeter-scale small displacement in the observation noise; therefore, they apply the orthogonal functions from the class of Gegenbauger polynomials and the orthogonal even functions. This method informs the foreboding of a destruction and will save many lives and infinite property of assets in catastrophic disasters after the present time.

The author believes these GNSS precise positioning technologies will bring better quality of life for our society near future.

2 CENTIMETER AUGMENETATION

2.1 Introduction

European Commission (EC) published *GNSS Market Report*, which is widely cited in the international community in GNSS area [8]. According to this report, the world's people have 7 billion GNSS devices for Location Based Service (LBS). The LBS devices adopt 3GPP standards, which are applied in popular mobile communication services. The PPP-RTK method is the precise point positioning in the RTK networks [9,10]. The author has developed Centimeter-class Augmentation System (CMAS) as a prototype demonstrator using the first satellite of QZSS and is pursuing more precise and faster convergence positioning in research and development until the present time.

In this chapter, the author addresses the design of GNSS PPP-RTK assistance system for 5G mobile networks and its algorithms for the first time in the world. There are past papers which described about PPP-RTK algorithms [11]. However, they are not systems for 5G mobile network and include accumulated programmatic inefficiency and excessive complication.

The author reveals theoretically essential meaning as system requirements and describe a principally operational flow[12], utilizing the heritage of application demonstrator for QZSS [13,14], and this content is quite useful for social implementation of the most advanced positioning infrastructure.

2.2 5G mobile network

5G mobile network is standardized in the 3GPP organization, which made the standards of 4th Generation (4G)/Long Term Evolution (LTE). Various regions of the world are launching 5G mobile services today. The 5G technology consists of both Enhanced LTE (eLTE) and New Radio (NR) which uses entirely novel techniques. The 3GPP made the international agreement for

adopting GNSS PPP-RTK service in 3GPP Release 16. It requires the precise positioning service with atmospheric correction using carrier-phase measurement and State Space Representation (SSR) [15,16].

The 3GPP mobile communication platform equips U-plane (User plane) and C-plane (Control plane), which are defined in its specifications. In particular, C-plane enables inner control for the network, and we can add the priority of service. The assistance data can be streamed through both planes.

The 5G mobile communication system is characterized by the performance of lower latency and larger capability. These features are also very useful and quite significant for precise positioning services

2.3 Design objective

The design objective is the highest performance of GNSS positioning system for mass-market applications using the latest technologies. Therefore, our target of this chapter is not a bidirectional service such as RTK or network RTK method, but a unidirectional service using broadcast channel such as a point pointing service.

In mobile networks, a bidirectional service needs a huge number of serving tasks, for example, tens of million transactions in a typical nation, but a unidirectional service only must serve by small number tasks. A unidirectional service is creating lower-cost higher-performance business.

2.3.1 Accuracy improvement

The existing system achieved the unidirectional correction across Japan [13]. This design also divides Japan into 12 areal networks shown as Fig. 2.3-1. Satellite clock and orbit errors physically do not depend on these areas, but ionospheric and tropospheric errors depend on the areas.

No	Area
1	West Hokkaido
2	East Hokkaido
3	North Tohoku
4	South Tohoku
5	Kanto
6	Hokuriku
7	Chubu
8	Kansai
9	Chugoku
10	Shikoku
11	North Kyushu
12	South Kyushu

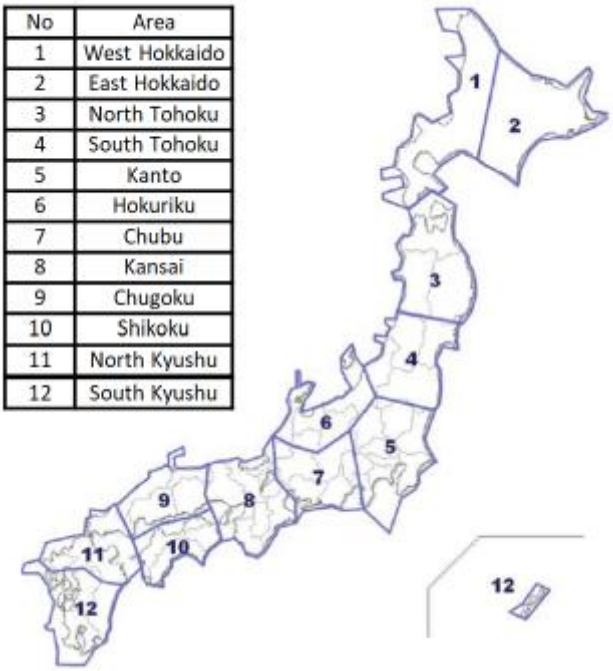

Fig. 2.3-1 Japanese Areal Networks in this design

The existing system calculates the common orbit error $\delta\bar{s}^p$ and the common clock error $\delta\bar{t}^p$ for the satellite "p" across Japan, due to the constraint of only one L6 signal capacity. The L6 signal is one of QZSS signals which distribute the SSR corrections for the CLAS services. It means the optimal clock error $\delta t_{o,a}^p$ and the optimal orbit error $\delta s_{o,a}^p$ in respective areal network "a", have added the adjustment factors $\epsilon_{t,a}$ and $\epsilon_{s,a}$ respectively such that

$$c\delta\bar{t}^p = c\delta t_{o,a}^p + \epsilon_{t,a}, \tag{1}$$

$$\delta\bar{s}^p = \delta s_{o,a}^p + \epsilon_{s,a}. \tag{2}$$

where, c is the light speed. In this case, "optimal" means to give a more accurate positioning result, focus on a positioning result, not clock or orbit accuracy, what the users do not need.

Therefore, the measured range error $\delta\rho_k^p$ at the reference station "*k* ", has the dilution of accuracy from the optimal range such that

$$\delta\rho_k^p = \delta\rho_{o,a}^p + \epsilon_{t,a} + \epsilon_{s,a}, \tag{3}$$

where $\delta\rho_k^p$ is the optimal value of the pseudorange error between the satellite "*p*" and the reference station "*k*".

5G's larger capacity overcomes this constraint with ease, and directly provides $\delta t_{o,a}^p$ and $\delta s_{o,a}^p$ into respective areal networks. It contributes to maximize the accuracy, by deriving from the supreme PPP-RTK potential.

We have checked it by the theory and the experiments. Namely, the proposed design adopts independent orbit and clock corrections for respective areal networks deriving the most optimizing power of the Kalman filter technique [19].

2.3.2 Convergence improvement

The existing system is constrained by the capacity of only one L6 satellite channel (1695bps) of QZSS. L6 satellite channel is used for Japan's original precise augmentation such as CLAS [14] and MADOCA [27]. The 5G's higher speed contributes to dramatically minimize the convergence time into a few seconds. The proposed design will check it by experiments.

2.4 Error models

The PPP-RTK assistance system identifies the errors through the algorithms and extracts distributed elements as follows.

$$\delta t^p,\ \delta s^p,\ \delta I_k^p,\ \delta \underline{T}_k,\ \delta b_C^p,\ \delta b_L^p,$$

where, δI_k^p is the ionospheric correction, $\delta \underline{T}_k$ is the zenith vertical tropospheric correction at the reference station *k*, δb_C^p is the code-phase biases, and δb_L^p is the carrier-phase biases for signal-in-space (SIS) for respective signals.

2.4.1 Satellite errors

Satellite errors consist of the orbit error and the clock error as follows

2.4.1.1 Satellite clock error

The total ranging error by clocks is represented as $c\delta t = c(\delta t_k - \delta t^p)$. As might be expected, the assistance system corrects for $-c\delta t^p$, and the receiver corrects for $c\delta t_k$, as the responsibility of respective parts in the system of positioning.

The satellite clock error is modeled by second order polynomial as a functional model, and white noise process as a stochastic model.

2.4.1.2 Satellite orbit error

The coordinate s^p of the satellite *p* and its integrated vector $\boldsymbol{s}$ are respectively denoted by

$$\boldsymbol{s} \equiv \begin{bmatrix} s^1 \\ s^2 \\ \vdots \\ s^{n_s} \end{bmatrix}, \quad s^p = \begin{bmatrix} x^p \\ y^p \\ z^p \end{bmatrix}. \tag{4}$$

The satellite orbit is modeled by cartesian elements as a function model and tridimensional Gauss-Markov process as a stochastic model.

In addition, the coordinate u_k of the position of the station k and its integrated vector $\boldsymbol{u}$ are respectively dented by

$$\boldsymbol{u} \equiv \begin{bmatrix} u_1 \\ u_2 \\ \vdots \\ u_{n_k} \end{bmatrix}, \quad u_k = \begin{bmatrix} x_k \\ y_k \\ z_k \end{bmatrix}. \tag{5}$$

The coordinate system is Earth-Centered Earth-Fixed (ECEF) for Eqs. (4) and (5). In practice, International Terrestrial Reference Frame (ITRF) is usually used. ITRF is specified in ISO 19161:2020. The orbit error $\delta\acute{s}_k^p$ on the line-of-sight from the satellite *p* to the station *k*, is represented as Eq. (6), where $\tilde{s}^p$ is a satellite position which is calculated from the broadcast ephemeris data.

$$\delta\acute{s}_k^p \equiv \frac{(u_k - s^p)^{\mathrm{T}}}{\|u_k - s^p\|}\{(u_k - s^p) - (u_k - \tilde{s}^p)\}. \tag{6}$$

Meanwhile, RTCM 10403.3 presents the orbits in the SSR form of radial, along-track, and cross-track components [16], therefore they must be transformed into the ECEF coordinate systems.

2.4.2 SIS biases

SIS biases consist of the code-phase bias δb_C^p and the carrier-phase bias δb_L^p, and the base signals are taken as L1C for GPS/QZSS and E1C for Galileo today. There are *C1* and *Cn* for code signals, and *L1* and *Ln* carrier-phase signals, where *n* = 2 or 5 for the second signals or bands.

2.4.2.1 Code-phase bias

For dual band, δb_C^p is defined as $\delta b_C^p \equiv \left[\delta b_{C1}^p \;\; \delta b_{Cn}^p\right]^{\mathrm{T}}$ and respective elements are such that

$$\delta b_{C1}^p = b_{C1}^p - b_{C1}^p = 0, \tag{7}$$

$$\delta b_{Cn}^{p} = b_{Cn}^{p} - b_{C1}^{p}, \tag{8}$$

where b_{C1}^{p} is the reference bias of the base signal.

The code-phase bias is modeled by a constant as a functional model, and integrated white noise process as a stochastic model.

2.4.2.2 Carrier-phase bias

Carrier-phase bias δb_{L}^{p} is defined as $\delta b_{L}^{p} \equiv \left[\delta b_{L1}^{p} \;\; \delta b_{Ln}^{p}\right]^{\mathrm{T}}$ and respective elements are such that

$$\delta b_{L1}^{p} = b_{L1}^{p} - b_{C1}^{p}, \tag{9}$$

$$\delta b_{Ln}^{p} = b_{Ln}^{p} - b_{C1}^{p}. \tag{10}$$

The carrier-phase bias is modeled by a constant as a functional model and integrated white noise process as a stochastic model.

2.4.3 Atmospheric errors

The atmospheric errors consist of the ionospheric error and the tropospheric error for centimeter positioning.

2.4.3.1 Ionospheric error

The ionospheric error δI_{k}^{p} is modeled as the slant total electron content (STEC) such that

$$\delta I_{k}^{p} = \delta I_{L1,k}^{p} = \frac{f_{Ln}^{2}}{f_{L1}^{2}} \delta I_{Ln,k}^{p}, \tag{11}$$

where, f_{L1} and f_{Ln} are respectively the frequencies of *L1* and *Ln* (*n*=2, 5) bands. There are other models of the vertical total electron content (VTEC) such as spherical harmonic and ball crown harmonic functions [34]. However, open PPP-RTK systems, which are such as QZSS CLAS and other SSR-distributed augmentation systems, adopt STEC as of now because of actual achievement.

The ionospheric error is modeled by a single layer polynomial (φ, λ) and one bias per satellite (vertical delay) as a functional model and tridimensional Gauss-Markov process (one bias per receiver-satellite combination) as a stochastic model.

2.4.3.2 Tropospheric error

The tropospheric error $\delta\underline{T}_k$ is modeled using the vertical zenith tropospheric model at the station *k*.

$$\delta\underline{T}_k \equiv \left[\, \delta\underline{T}_{H,k} \quad \delta\underline{T}_{M,k} \,\right]^{\mathrm{T}}, \tag{12}$$

where, $\delta\underline{T}_{H,k}$ is the hydrostatic component, $\delta\underline{T}_{M,k}$ is the moisture component. We apply Saastaimonen's tropospheric model $Z(h,t)$ [17] and Neil's mapping function $M\left(E_k^p\right)$ [18], and E_k^p is an elevation angle, h is a height above the sea level. The slant tropospheric errors δT_k^p is calculated from the zenith vertical tropospheric error $\delta\underline{T}_k$ as follows.

$$\begin{aligned}
\delta T_k^p &= M\left(E_k^p\right) Z(h,t)\delta\underline{T}_k \\
&= \left[M_H\left(E_k^p\right) \quad M_H\left(E_k^p\right)\right]\begin{bmatrix} \dfrac{Z_H(h,t)}{Z_H(0,t)} & 0 \\ 0 & \dfrac{Z_M(h,t)}{Z_M(0,t)} \end{bmatrix}\delta\underline{T}_k \\
&= M_H\left(E_k^p\right)\frac{Z_H(h,t)}{Z_H(0,t)}\delta\underline{T}_{H,k} + M_M\left(E_k^p\right)\frac{Z_M(h,t)}{Z_M(0,t)}\delta\underline{T}_{M,k}\,.
\end{aligned} \tag{13}$$

The troposphere error is modeled by the above formula as a functional model and two scaling parameter per station as a stochastic model.

2.4.4 Receiver-corrected errors

The station residual error $e_{f,k}^{p}$ which the assistance system does not distribute, is described as Eq. (14) where *f* is the signal code or the signal frequency of carrier-phase. The right-hand side includes the parameters calculated by physical theories and/or measured in advance [14].

$$e_{f,k}^{p} = \delta M_{k}^{p} + e_{A,f,k} + e_{E,k} + e_{R,k}^{p} + e_{D,f,k}, \tag{14}$$

where

δM_{k}^{p} : multipath and auxiliary error,

$e_{A,f,k}$: antenna phase center difference,

$e_{E,k}$: earth tide error,

$e_{W,k}$: carrier-phase wind up error,

$e_{R,k}^{p}$: relativity error,

$e_{D,f,k}$: station residual error.

The antenna phase center difference of a receiver is taken by calibration as a functional model.

The multipath about a receiver is modeled by elevation dependent weighting as a functional model, and first order Gauss-Markov process as a stochastic model. A receiver has signal delay which is modeled by constant as a functional model, and integrated white noise process as a stochastic model. In general terms, the measurement noise is modeled by white noise process.

2.5 Observation equation

The observation equation is described as follows, and configurated the Kalman filter [19] to generate the accurate correction parameters .

The observation equation is as follows. The pseudoranges $\rho_{C1,k}^{p}$ and $\rho_{Cn,k}^{p}$ of signal code *C*1 and *Cn* (*n* = 2 or 5) respectively, are described Eqs. (15) and (16).

$$\rho_{C1,k}^{p} = r_k^p + \delta\acute{s}_k^p + c(\delta t_k - \delta t^p) + \delta I_k^p + \delta T_k^p + \delta b_{C1}^p + e_{C1,k}^p \,, \tag{15}$$

$$\rho_{Cn,k}^{p} = r_k^p + \delta\acute{s}_k^p + c(\delta t_k - \delta t^p) + \frac{f_{L1}^2}{f_{Ln}^2}\delta I_k^p + \delta T_k^p + \delta b_{Cn}^p + e_{Cn,k}^p \,, \tag{16}$$

where, r_k^p is the geometric range between the satellite *p* and the receiver station *k*, and $e_{C1,k}^{p}$ and $e_{Cn,k}^{p}$ are the residual errors respectively for the *C1* and *Cn* signals.

The phaserange $\Phi_{L1,k}^{p}$ and $\Phi_{Ln,k}^{p}$ with signal frequency *L*1 and *Ln* (*n* =2 or 5) are represented as Eqs. (17) and (18).

$$\Phi_{L1,k}^{p} = r_k^p + \delta\acute{s}_k^p + c(\delta t_k - \delta t^p) + \delta I_k^p + \delta T_k^p + \delta b_{L1}^p + \lambda_{L1} N_{L1,k}^p + e_{L1,k}^p \,, \tag{17}$$

$$\Phi_{Ln,k}^{p} = r_k^p + \delta\acute{s}_k^p + c(\delta t_k - \delta t^p) + \frac{f_{L1}^2}{f_{Ln}^2}\delta I_k^p + \delta T_k^p + \delta b_{Ln}^p + \lambda_{Ln} N_{Ln,k}^p + e_{Ln,k}^p \,, \tag{18}$$

where, $N_{L1,k}^{p}$ and $N_{Ln,k}^{p}$ are wave number integer biases of satellite-to-receiver, and λ_{L1} and λ_{Ln} are the wavelength of *L*1-band and *Ln*-band respectively (*n* = 2 or 5). $e_{L1,k}^{p}$ and $e_{Ln,k}^{p}$ are the residual errors respectively for the *L1* and *Ln* signals.

2.6 System design

In this section, we show the design and the algorithms as the system requirement for 5G GNSS PPP-RTK assistance system using the Kalman filter. $\bar{u}_k$ is the average of the positional solutions of each day for two weeks on moving earth crust as the reference position of the station *k*. The positional solution of each day is provided from Geospatial Information Authority (GSI) of Japan, as the nationally authorized reference position of the GEONET station *k*. GEONET is the national Continuously Operating Reference Station (CORS) network. The displacement of the station *k* from the reference position is represented such that

$$\delta u_k = u_k - \bar{u}_k. \tag{19}$$

It means to fit with the temporal epoch coordinates of Japanese Geodetic Datum 2011 (JGD2011), that is the basis of transformation to the reference epoch of JGD2011, the right national coordinate system, which is required in the practical market, for example, to build the smart cities as the national projects.

The precise estimate $\hat{\rho}_k^p$ of the phaserange can be calculated such that

$$\hat{\rho}_k^p = \Phi_{L1,k}^p - \left\{\delta\hat{s}_k^p + c(\delta\hat{t}_k - \delta\hat{t}^p) + \delta\hat{I}_k^p + \delta\hat{T}_k^p + \delta\hat{b}_{L1}^p + \lambda_{L1}\widehat{N}_{L1,k}^p + \hat{e}_{L1,k}^p\right\}. \tag{20}$$

where, $\hat{e}_{L1,k}^p$ is the residual error. The hat symbol means the optimal estimate of respective valuables. Eq. (20) is derived from Eq. (15) and Eq. (17).

2.6.1 Observation dimension

We must check the dimension n_y of the observation space. The system nominally uses 25 stations per a network of the assistance system. 12 satellites are typically received. The respective satellites are used as 2 signals with 2 channels such as code and carrier-phase. Therefore,

$$n_y = 25 \times 12 \times 2 \times 2 = 1200 \text{ dimensions.} \tag{21}$$

The whole land of Japan is divided to 12 networks as Fig. 2.3-1. Therefore, the total dimension is such that

$$n_y^{Japan} = 1200 \times 12 = 14000 \text{ dimensions.} \tag{22}$$

The dimension is practically time-variant depending on operations of satellite and CORS status in action.

2.6.2 State equation

The author designs to optimize the area networks respectively and makes a model of one network using all stations in the network [14]. From Eqs. (15)-(18), the state equations represented as Eqs. (23) and (24) are configurated [10].

$$\boldsymbol{\theta}_{t+1} = \boldsymbol{F}\,\boldsymbol{\theta}_t + \boldsymbol{G}\,\boldsymbol{w}_t, \tag{23}$$
$$\boldsymbol{y}_t = \boldsymbol{H}_t\boldsymbol{\theta}_t + \boldsymbol{v}_t, \tag{24}$$

The observation vector and the state vector, where all components are written as sub-vector, are rather complicated and therefore they can be represented as only summarized sets of sub-vectors.

$$\boldsymbol{y}_t \equiv \begin{bmatrix} \boldsymbol{y}_{1,t} \\ \boldsymbol{y}_{2,t} \\ \vdots \\ \boldsymbol{y}_{n_k,t} \end{bmatrix}, \quad \boldsymbol{y}_{k,t} \equiv \begin{bmatrix} \boldsymbol{\delta\rho}_{C1,k} \\ \boldsymbol{\delta\rho}_{Cn,k} \\ \boldsymbol{\delta\Phi}_{L1,k} \\ \boldsymbol{\delta\Phi}_{Ln,k} \end{bmatrix}, \tag{25a}$$

$$\boldsymbol{\delta\rho}_{C1,k} \equiv \begin{bmatrix} \delta\rho_{C1,k}^{1} \\ \delta\rho_{C1,k}^{2} \\ \vdots \\ \delta\rho_{C1,k}^{n_s} \end{bmatrix}, \quad \boldsymbol{\delta\rho}_{Cn,k} \equiv \begin{bmatrix} \delta\rho_{Cn,k}^{1} \\ \delta\rho_{Cn,k}^{2} \\ \vdots \\ \delta\rho_{Cn,k}^{n_s} \end{bmatrix}, \quad \boldsymbol{\delta\Phi}_{L1,k} \equiv \begin{bmatrix} \delta\Phi_{L1,k}^{1} \\ \delta\Phi_{L1,k}^{2} \\ \vdots \\ \delta\Phi_{L1,k}^{n_s} \end{bmatrix}, \quad \boldsymbol{\delta\Phi}_{Ln,k} \equiv \begin{bmatrix} \delta\Phi_{Ln,k}^{1} \\ \delta\Phi_{Ln,k}^{2} \\ \vdots \\ \delta\Phi_{Ln,k}^{n_s} \end{bmatrix}, \tag{25b}$$

$$\boldsymbol{\theta}_t \equiv \begin{bmatrix} \boldsymbol{\delta u} \\ \boldsymbol{\delta t_s} \\ \boldsymbol{\delta s} \\ \boldsymbol{\delta I} \\ \boldsymbol{\delta T} \\ \boldsymbol{N} \\ \boldsymbol{\delta t_u} \\ \boldsymbol{\delta M} \end{bmatrix}, \tag{26a}$$

$$\boldsymbol{\delta u} \equiv \begin{bmatrix} \delta u_1 \\ \delta u_2 \\ \vdots \\ \delta u_{n_k} \end{bmatrix}, \quad \boldsymbol{\delta s} \equiv \begin{bmatrix} \delta s^1 \\ \delta s^2 \\ \vdots \\ \delta s^{n_s} \end{bmatrix}, \quad \boldsymbol{\delta t_s} \equiv \begin{bmatrix} \delta t^1 \\ \delta t^2 \\ \vdots \\ \delta t^{n_s} \end{bmatrix}, \quad \boldsymbol{\delta t_u} \equiv \begin{bmatrix} \delta t_1 \\ \delta t_2 \\ \vdots \\ \delta t_{n_k} \end{bmatrix}, \tag{26b}$$

$$\boldsymbol{\delta I} \equiv \begin{bmatrix} \delta I_1^1 \\ \delta I_1^2 \\ \vdots \\ \delta I_1^{n_s} \\ \delta I_2^1 \\ \vdots \\ \delta I_k^p \\ \vdots \\ \delta I_{n_k-1}^{n_s} \\ \delta I_{n_k}^1 \\ \delta I_{n_k}^2 \\ \vdots \\ \delta I_{n_k}^{n_s} \end{bmatrix}, \quad \boldsymbol{\delta T} \equiv \begin{bmatrix} \delta T_1^1 \\ \delta T_1^2 \\ \vdots \\ \delta T_1^{n_s} \\ \delta T_2^1 \\ \vdots \\ \delta T_k^p \\ \vdots \\ \delta T_{n_k-1}^{n_s} \\ \delta T_{n_k}^1 \\ \delta T_{n_k}^2 \\ \vdots \\ \delta T_{n_k}^{n_s} \end{bmatrix}, \quad \boldsymbol{\delta N} \equiv \begin{bmatrix} \delta N_1^1 \\ \delta N_1^2 \\ \vdots \\ \delta N_1^{n_s} \\ \delta N_2^1 \\ \vdots \\ \delta N_k^p \\ \vdots \\ \delta N_{n_k-1}^{n_s} \\ \delta N_{n_k}^1 \\ \delta N_{n_k}^2 \\ \vdots \\ \delta N_{n_k}^{n_s} \end{bmatrix}, \quad \boldsymbol{\delta M} \equiv \begin{bmatrix} \delta M_1^1 \\ \delta M_1^2 \\ \vdots \\ \delta M_1^{n_s} \\ \delta M_2^1 \\ \vdots \\ \delta M_k^p \\ \vdots \\ \delta M_{n_k-1}^{n_s} \\ \delta M_{n_k}^1 \\ \delta M_{n_k}^2 \\ \vdots \\ \delta M_{n_k}^{n_s} \end{bmatrix}. \tag{26c}$$

The state equation includes stochastic valuables with variance such that

$$E[\boldsymbol{w}_t \boldsymbol{w}_\tau] = \boldsymbol{Q}_t \boldsymbol{\delta}_{ij}, \tag{26d}$$
$$E[\boldsymbol{v}_t \boldsymbol{v}_\tau] = \boldsymbol{R}_t \boldsymbol{\delta}_{ij}, \tag{26c}$$

where, $\boldsymbol{w}_t$ and $\boldsymbol{v}_t$ are independent Gaussian white noise, $\boldsymbol{\delta}_{ij}$ is the Kronecker's δ-function at the time *t*. N_k^p is defined as

$$N_k^p \equiv \begin{bmatrix} N_{L1,k}^p & N_{Ln,k}^p \end{bmatrix}^{\mathrm{T}}$$

The state vector does not include δb_C^p and δb_L^p, and these parameters are calculated out of the Kalman filtering optimization.

In one computational task, there are n_s satellites and n_k stations. Therefore, the dimensions of the state valuables are

$$u_k\colon 3n_k,\ \delta t^p\colon n_s,\ \delta s^p\colon 3n_s,\ \delta I_k^p\colon n_s n_k,\ \delta T_k^p\colon n_s n_k,\ N_k^p\colon 2n_s n_k,\ t_k\colon n_k,\ \delta M_k^p\colon n_s n_k.$$

The matrix *F* and *G* of the Kalman filter [18] are represented such that

$$\boldsymbol{F} = \begin{bmatrix} I_{n_a} \end{bmatrix} \tag{27a}$$
$$\boldsymbol{G} = \begin{bmatrix} I_{n_a} \end{bmatrix} \tag{27b}$$

where,

$$n_a = 3n_k + n_s + 3n_s + n_s n_k + 2n_s n_k + n_k + n_s n_k \tag{27c}$$

The matrix $\boldsymbol{H}_t$ in the Kalman filter is represented such that

$$\boldsymbol{H}_t \equiv \begin{bmatrix} H_{1,t} \\ H_{2,t} \\ \vdots \\ H_{n_k,t} \end{bmatrix}, \tag{28a}$$

$$H_{k,t} = \begin{bmatrix} g_k^p I_{n_s} & c\, I_{n_s} & g_k^p\, I_{n_s} & J_k & J_k & O_{n_s n_k} & -c\, I_{n_s} & J_k \\ g_k^p I_{n_s} & c\, I_{n_s} & g_k^p\, I_{n_s} & \frac{f_{L1}^2}{f_{Ln}^2} J_k & J_k & O_{n_s n_k} & -c\, I_{n_s} & J_k \\ g_k^p I_{n_s} & c\, I_{n_s} & g_k^p\, I_{n_s} & -J_k & J_k & \lambda_{L1}\, J_k & -c\, I_{n_s} & J_k \\ g_k^p I_{n_s} & c\, I_{n_s} & g_k^p\, I_{n_s} & -\frac{f_{L1}^2}{f_{Ln}^2} J_k & J_k & \lambda_{Ln}\, J_k & -c\, I_{n_s} & J_k \end{bmatrix}, \tag{28b}$$

where, I_n is the unit matrix of order *n*, O_n is the zero matrix of order *n*, and the linearized coefficient g_k^p in the matrix $\boldsymbol{H}_t$ is defined using the reference position $\bar{u}_k$ of the station *k* such that

$$g_k^p \equiv \left[\frac{\partial \bar{r}_k^p}{\partial u_k}\right]^{\mathrm{T}}_{u_k=\bar{u}_k} = \left[\frac{\bar{x}_k - x^p}{\bar{r}_k^p}, \frac{\bar{y}_k - y^p}{\bar{r}_k^p}, \frac{\bar{z}_k - z^p}{\bar{r}_k^p}\right], \tag{29a}$$

$$\bar{r}_k^p \equiv \| \bar{u}_k - s^p \|. \tag{29b}$$

The matrix J_k has a special form such that

$$J_k = [J_1 \quad \cdots \quad J_i \quad \cdots \quad J_{n_k}], \tag{30a}$$

$$J_i \equiv \begin{cases} I_{n_s} & (i = k) \\ O_{n_s} & (i \neq k) \end{cases}. \tag{30b}$$

In actual calculation, multiplying zero does not execute for example, because the calculation power must be exercise economy. The actual calculation is rather complicated; therefore, the above equations can be represented as organized mathematical principle.

2.6.3 Computability

We need to check the independent dimension of the state space. n_s satellites and n_k stations are used per region which one computational task covers.

$$u_k\colon 3n_k,\ \delta t^p\colon n_s,\ \delta s^p\colon 3n_s,\ \delta I_k^p\colon n_s n_k,\ \delta \underline{T}_k\colon 2n_k,\ t_k\colon n_k,\ \delta M_k^p\colon n_s n_k.$$

Despite being the state vector element, $N_{L1,k}^p$ and $N_{Ln,k}^p$ do not become independent dimension such that

$$\lambda_{L1}N_{L1,k}^{p} = \rho_{k}^{p} - \{r_{k}^{p} - \delta I_{L1,k}^{p} + \delta T_{k}^{p} + c(\delta t_{k} - \delta t^{p}) + \delta b_{L1}^{p} + e_{L1,k}^{p}\}, \quad (31)$$

$$\lambda_{Ln}N_{Ln,k}^{p} = \rho_{k}^{p} - \{r_{k}^{p} - \delta I_{Ln,k}^{p} + \delta T_{k}^{p} + c(\delta t_{k} - \delta t^{p}) + \delta b_{Ln}^{p} + e_{Ln,k}^{p}\}. \quad (32)$$

where, $e_{L1,k}^{p}$ and $e_{Ln,k}^{p}$ are the residual errors respectively for the *L1* and *Ln* signals of ranging. Because of n_k=25 and n_s=12, the independent dimension of the state space can be calculated as follows.

$$n_c = 3 \times 25 + 12 + 3 \times 12 + 12 \times 25 + 2 \times 25 + 25 + 12 \times 25 = 798 \text{ dimensions.} \quad (33)$$

Therefore, the total dimension for Japan is

$$n_c^{Japan} = 798 \times 12 = 9\,576 \text{ dimensions.} \quad (34)$$

Because of $n_y > n_c$, the computation is possible, and the system can give the solutions.

2.6.4 Kalman filtering

2.6.4.1 Update operation

The filtering and prediction, the Kalman gain $\boldsymbol{K}_t$, and the estimated error covariance $\boldsymbol{\Sigma}_{t|t-1}$ are obtained such that

$$\widehat{\boldsymbol{\theta}}_{t+1|t} = \boldsymbol{F}\,\widehat{\boldsymbol{\theta}}_{t|t}, \quad (35)$$

$$\widehat{\boldsymbol{\theta}}_{t|t} = \widehat{\boldsymbol{\theta}}_{t|t-1} + \boldsymbol{K}_t\left[\boldsymbol{y}_t - \boldsymbol{H}_t\,\boldsymbol{\theta}_{t|t-1}\right], \quad (36)$$

$$\boldsymbol{K}_t = \boldsymbol{\Sigma}_{t|t-1}\boldsymbol{H}_t^{\mathrm{T}}\left[\boldsymbol{H}_t\,\boldsymbol{\Sigma}_{t|t-1}\boldsymbol{H}_t^{\mathrm{T}} + \boldsymbol{R}_t\right]. \quad (37)$$

The assistance systems run continuously, and operators usually maintain its services with checking realtime valuables on its continuous operation.

2.6.4.2 Initial conditions

The initial conditions for the Kalman filter are provided from the navigation messages from GNSS, the GEONET positions given in advance, and the precise ephemeris data from the expertized agencies in the world through the internet. These parameters use into the initial state valuable $\overline{\boldsymbol{\theta}}_0$ and the initial variance $\boldsymbol{P}_0$. In particular, the precise ephemeris data reflect onto the initial δt^p and δs^p of the components of $\overline{\boldsymbol{\theta}}_0$.

$$E[\boldsymbol{\theta}_0] = \widehat{\boldsymbol{\theta}}_{0|-1} = \overline{\boldsymbol{\theta}}_0, \quad \mathrm{Var}[\boldsymbol{\theta}_0] = \boldsymbol{\Sigma}_{0|-1} = \boldsymbol{P}_0. \tag{38}$$

The assistance systems run in 24 hours on 365 days, and the initial condition transfers its steady condition.

2.7 Assistance service

The assistance system generates $\widehat{\boldsymbol{\theta}}_{t|t}$ through the above algorithms and extracts distributed elements.

$$\delta\hat{t}^p,\ \delta\hat{s}^p,\ \delta\hat{b}_C^p,\ \delta\hat{b}_L^p,\ \delta\hat{I}_k^p\ ,\ \delta\underline{\hat{T}}_k\ .$$

2.7.1 Atmospheric grid

The estimated atmospheric errors $\delta\hat{I}_k^p$ and $\delta\underline{\hat{T}}_k$ must be transformed into the value at the horizontal position *k'* which the user receiver knows, because the receivers do not know the

station's horizontal position *k*. Therefore, the grid's horizontal position *k'* is defined. This method has the below merits.

(1) Independent from changing station network

(2) No need to publish the station positions

In particular, the item (2) may be important for the countries concerning the national security.

The PPP-RTK technique uses the grid set which covers its service area. The station's position *k* is transformed to the grid's position *k'*. k_1, k_2, k_3 and k_4 are the positions around the position *k'* and d_1, d_2, d_3 and d_4 are the distance of k_1, k_2, k_3 and k_4 from the position *k'*. $\delta\hat{I}^p_{k'}$ and $\delta\hat{\underline{T}}_{k'}$ are represented such that

$$\delta\hat{I}^p_{k'} = \sum_{j=1}^{4} W_{I,k_j}\, \delta\hat{I}^p_{k_j}, \tag{39a}$$

$$\delta\hat{\underline{T}}_{k'} = \sum_{j=1}^{4} W_{T,k_j}\, \delta\hat{\underline{T}}_{k_j}, \tag{39b}$$

where, W_{I,k_j} and W_{T,k_j} are weight coefficients. The interpolation of this part is possible to take other formulae depending on designers or tools [13].

2.7.2 Distribution

The PPP-RTK corrections are distributed shown as Table 2.7-1. Δt_{QZ} is the interval time by the existing system [14] and Δt_{5G} by the 5G platform. This table shows that the PPP-RTK services on 5G can achieve very short interval, because higher speed communication and enough capacity. The distribution is easy even at 30 times data capacity to the user receivers.

Table 2.7-1 Distributed corrections

Correction	Symbol	Δt_{QZ}	Δt_{5G}
Satellite clock correction	$\delta\hat{t}^p$	5 s	1 s
Satellite orbit correction	$\delta\hat{s}^p$	30 s	
SIS code-phase bias	$\delta\hat{b}_C^p$		
SIS carrier-phase bias	$\delta\hat{b}_L^p$		
Ionospheric correction	$\delta\hat{I}_k^p$		
Tropospheric correction	$\delta\underline{\hat{T}}_k$		

The practical system distributes the parameters of user range accuracy (URA) [14] and proposes an authentication message for anti-spoofing for future applications [13].

The precise estimates $\widehat{\Phi}_{L1,k}^p$ and $\widehat{\Phi}_{Ln,k}^p$ of the phaserange can be calculated such that

$$\hat{\rho}_{C1,k}^p = \rho_{C1,k}^p - \{\delta\hat{s}_k^p + c(\delta\hat{t}_k - \delta\hat{t}^p) + \delta\hat{I}_k^p + \delta\hat{T}_k^p + \delta\hat{b}_{C1}^p + \hat{e}_{C1,k}^p\}, \quad (40a)$$

$$\hat{\rho}_{Cn,k}^p = \rho_{Cn,k}^p - \left\{\delta\hat{s}_k^p + c(\delta\hat{t}_k - \delta\hat{t}^p) + \frac{f_{L1}^2}{f_{Ln}^2}\delta\hat{I}_k^p + \delta\hat{T}_k^p + \delta\hat{b}_{Cn}^p + \hat{e}_{Cn,k}^p\right\}, \quad (40b)$$

$$\widehat{\Phi}_{L1,k}^p = \Phi_{L1,k}^p - \{\delta\hat{s}_k^p + c(\delta\hat{t}_k - \delta\hat{t}^p) - \delta\hat{I}_k^p + \delta\hat{T}_k^p + \delta\hat{b}_{L1}^p + \lambda_{L1}\widehat{N}_{L1,k}^p + \hat{e}_{L1,k}^p\}, \quad (40c)$$

$$\widehat{\Phi}_{Ln,k}^p = \Phi_{Ln,k}^p - \left\{\delta\hat{s}_k^p + c(\delta\hat{t}_k - \delta\hat{t}^p) - \frac{f_{L1}^2}{f_{Ln}^2}\delta\hat{I}_k^p + \delta\hat{T}_k^p + \delta\hat{b}_{Ln}^p + \lambda_{Ln}\widehat{N}_{Ln,k}^p + \hat{e}_{Ln,k}^p\right\}. \quad (40d)$$

3 EXPERIMENTS FOR CENTIMETER AUGMENTATION

3.1 Experiments of accuracy and convergence

The experiments of the designed assistance system and its algorithms were carried out. The observation data were sent from 25 stations of GEONET per one region of approximately 200 by 200 kilometers. In the experiments, we measured the accuracy and the convergence time of the positioning result using the GNSS PPP-RTK assistance system based on the QZSS Centimeter-class Augmentation System (CLAS), which is a prototype demonstration system of practical CLAS system.

3.1.1 Positioning accuracy

The measured point was Tokyo-metropolitan Authorized Refence Point 10A58 near the Emperor Palace shown as Table 3.1-1. The dual frequency signals of GPS were utilized in the experiment. The receiver was the Mitsubishi LEXR receiver. In this case, we used only GPS constellation for evaluating the algorithms. Table 3.1-2, Fig. 3.1-1 and 3.1-2 show the test result of horizontal and height accuracies.

Table 3.1-1 Test conditions of positioning accuracy

No	Item	Content
1	Point	10A58
2	Positioning Terminal	LEXR/Software
3	Date	November 27th , 2018
4	Time	14:22:49 - 14:29:59

Table 3.1-2 Test result of positioning accuracy

No	Item	2D	Height	Unit
1	Standard deviation	0.71	1.15	cm
2	Bias	0.93	0.64	cm
3	RMSE	1.01	1.32	cm

In Fig. 3.1-1, the directions are given by the standard of the Ministry of Land, Infrastructure and Tourism (MLIT) of Japan, that the upward is north and the rightward is east.

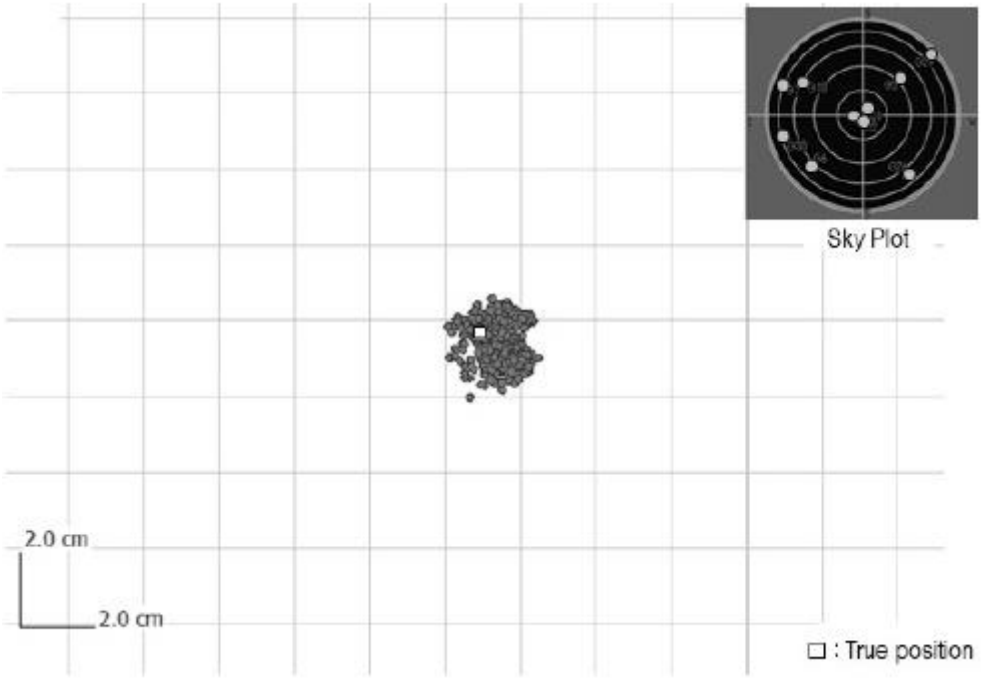

Fig. 3.1-1 Test Result of Horizontal Accuracy on North-East Plane

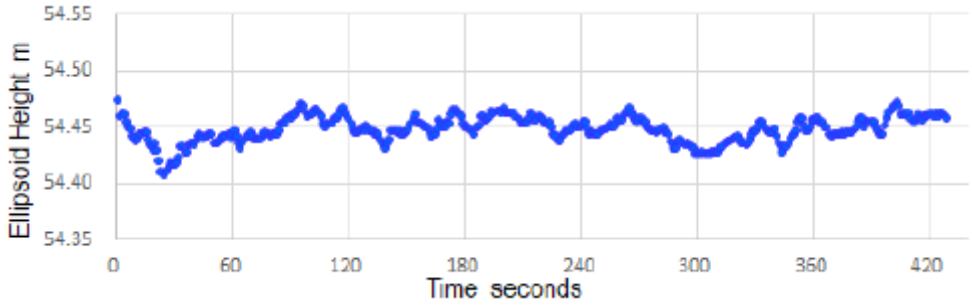

Fig. 3.1-2 Test Result of Height Measurement

The accuracy 1.01 [cm] (drms) in the horizontal direction and 1.32 [cm] (rms) in the vertical direction were obtained, where “drms” is the distance root mean square, and “rms” is root mean square. Furthermore, the fix rate was 99.5 [%]. The fix rate is the percentage of fixing the integer ambiguity of the carrier-wave number. We can evaluate these are an equivalent level to the result of network RTK GNSS positioning method.

3.1.2 Convergence time

The convergence time is defined in this thesis as a time from the beginning of positioning to 100 [%] of ambiguity fixing in the 7 GEONET station receiver of 10 cases. Table 3.1-3 is the test conditions, and Fig. 3.1-3 shows the test result.

Table 3.1-3 Test conditions of convergence time

No	Item	Content
1	Average	10 cases
2	Receiver	7 GEONET stations
3	Region	Kanto
4	Date	February 4th, 2018

In Fig. 3.1-3, the red line is the average of 10 cases, which are the test cases of the 7 GEONET stations, which are deemed receivers. The accumulated fix rate is the percentage of ambiguity fixing.

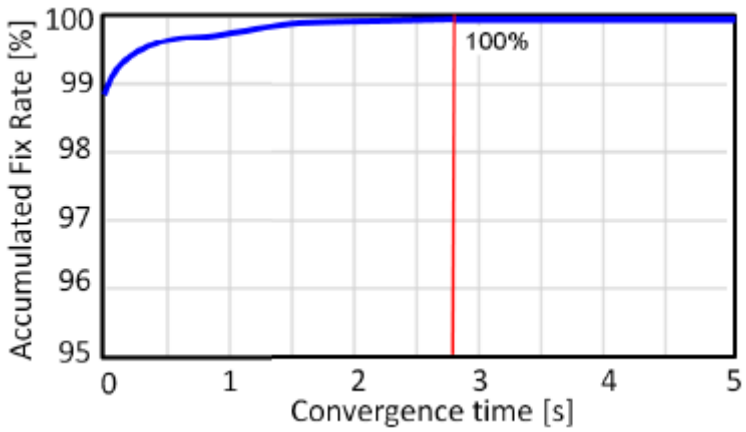

Fig. 3.1-3 Test Result of Convergence Time

The reason that we use the GEONET stations as deemed receivers, is that ideal receivers are needed for testing the assistance system to distinguish the performances between the assistance system and the user receivers.

It is evaluated these are an equivalent level to the result of network RTK GNSS positioning method.

3.1.3 Experimental summary

Compared with the existing system [14], this design makes the drms from 3.57 [cm] to 1.01 [cm], the height rms from 6.13 [cm] to 1.32 [cm], the convergence time from 60.0 [s] to 2.8 [s]. It can be said the highest performance as the unidirectional assistance of real-time GNSS positioning today.

Table 3.1-4 Comparison of performance

Performance		Existing System	Proposed Design	Unit
Accuracy (rms)	2D	3.57	1.01	cm
	Height	6.13	1.32	cm
Convergence time		60.0	2.8	s

The convergence time of QZSS CLAS is one minute. The conventional 4G/LTE communication has 4 to 5 [s] delay, therefore total convergence time become 6 to 7 [s]. The CLAS-type positioning augmentation systems using 4G/LTE is not provided yet at the present time, The proposed system can make to realize a half convergence time. It is very useful for both consumer and professional users.

3.2 Conclusion for Centimeter Augmentation

In Chapter 2 and 3,the author shows the design of a new GNSS PPP-RTK assistance system using the 5G excellences, based on the QZSS heritage. In the comparison with the existing system [8], this design improves the horizontal accuracy from 3 [cm] to approximately 1 [cm], the convergence time from 60 [s] to approximately 3 [s]. This is the highest performance as the unidirectional assistance system of real-time GNSS positioning for mass-market applications which should be implemented into the next-generation smart societies.

4 MILLIMETER DISPLACEMENT DETCTION

4.1 Introduction

The Ministry of Land, Infrastructure, Transport and Tourism (MLIT) of Japan has been warning 525 thousand places in danger of landslide sediment disasters in Japan [20, 21].

Industrial companies provide GNSS detection systems and services for this problem. GNSS precise sensors were, however, expensive in past years, and a data-analyzing time is long, 24 [h] in the existing services. Therefore, more rapid detection is strongly required. On the other hand, the latest GNSS sensors are low-cost and high performance. Therefore, a new and effective solution has been expected.

In order to respond this need, we develop a new principle of mathematical algorithms for detecting a destructive displacement from GNSS precise positioning observation. The algorithms must retrieve a millimeter-scale positional change which is modelled as a step function in observation noise of GNSS precise positioning system. The author and his associates describe outline and effect in our past papers [22,23]. This thesis reveals a detailed mechanism and mathematical algorithms clearly.

4.2 Models of problem

A destructive displacement is a discontinuous phenomenon that occurs in a landslide of slopes and a constructional collapse of bridges and buildings. In this section, we define a displacement model and a measurement model for this problem and show a scope of GNSS techniques which we can use. Japanese GNSS, Quasi-Zenith Satellite System (QZSS) [3,14] also can be applied to this method.

4.2.1 Displacement model

In Japan, more than 20 industrial companies of civil engineering have established the Shamen-net Study Group and promote to research the displacement measurement using GNSS. They adopt the step function for the destructive displacement model, and the analysis divides each dimension for simplicity [24].

A landslide and a constructional collapse are phenomena which occur in the 3-dimensional space. But a direction of landslide or collapse is known in advance. Because the direction of falling by the gravity is determined in actual places. Therefore, we treat it as 1-dimensional problem in this thesis.

We define the displacement function $s_D(t)$ [mm] that a step-shaped displacement occurs at the time t_D [s] as Eq. (41) and Fig. 4.2-1.

$$s_D(t) = \begin{cases} \mu_0 & [\text{mm}] \quad (t < t_D\ [s]), \\ \mu_1 = \mu_0 + \Delta\mu & [\text{mm}] \quad (t \geq t_D\ [s]). \end{cases} \tag{41}$$

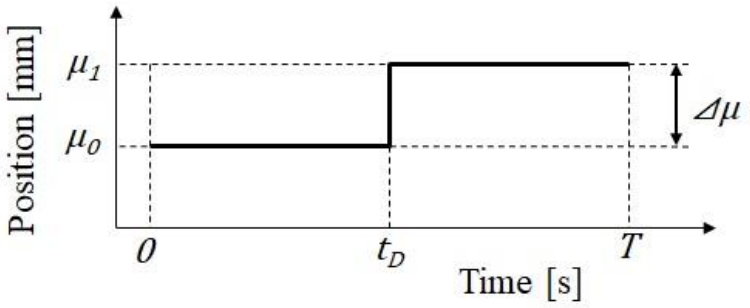

Fig. 4.2-1 Displacement model $s_D(t)$

In Fig. 4.2-1, $\Delta\mu$ [mm] is the position before the displacement, μ_1[mm] is the position after the displacement, the start time of measurement is 0 [s] the end time is T [s]. The displacement function $s_D(t)$ makes the displacement length $\Delta\mu$ [mm] at the time t_D [s].

4.2.2 Measurement model

The measurement data of GNSS positioning $x(t)$ [mm] are the sum of the displacement function $s_D(t)$ [mm] and the observation noise $w(t)$ [mm] shown as

$$x(t) = s_D(t) + w(t) \text{ [mm]}. \tag{42}$$

The problem of this article is to find the occurrence time t_D [s] and displacement $\Delta\mu$ [mm] by retrieving the displacement function $s_D(t)$ [mm] from the measurement data $x(t)$ [mm] with observation noise $w(t)$ [mm].

This is the so-called second level problem of Van Trees [18] which detects a signal with unknown parameters among noises. In this case, unknown parameters are the occurrence time t_D [s] and displacement $\Delta\mu$ [mm].

The basis of signal detection and estimation for radars and sonars is given by Harry L. Van Trees [18]. But major countries have deployed new generation GNSS systems by 2020, and the characteristics of millimeter-scale positioning is not known well yet.

In particular, it is a large problem to find rapidly millimeter-scale displacement using the ranging signals transmitted by the navigation satellites which are more distant than 20 thousand kilometers. This study presents the algorithms which make it possible.

4.2.3 Scope of GNSS techniques

In this section, we clarify a scope of GNSS technique which can be applied by these detection algorithms. Regarding millimeter displacement detection, we need entirely different from centimeter positioning, in the view of purpose, accuracy, and target models. Therefore, we consider GNSS precise positioning using carrier-phase fundamentally on its head.

These algorithms are used to centimeter-class measurement data which include the pseudorange $\rho_{i,u}^{p}(t)$ and the carrier-phase $\phi_{i,u}^{p}(t)$ of the ranging signal of L-band *i*-th frequency at the time *t* from the satellite *p* to the user receiver *u*. When the integer biases of the carriers have been solved, the phase-range $\Phi_{i,u}^{p}(t)$ is represented by

$$\Phi_{i,u}^{p}(t) = \lambda_i \phi_{i,u}^{p}(t), \tag{43}$$

where λ_i is the wavelength of the ranging signal of *i*-th frequency of L-band. The pseudorange, the carrier-phase, and the phase-range are specified in RTCM Standard 10403.3 [15]. The pseudorange and the phase-range are represented as follows [25].

Pseudorange $\rho_{i,u}^{p}$:

$$\rho_{i,u}^{p}(t) = \gamma_u^p\left(t, t-\tau_u^p\right) + c\left\{\delta t_u(t) - \delta t^p\left(t-\tau_u^p\right)\right\} + \frac{f_1^2}{f_i^2}\delta I_u^p(t) + \delta T_u^p(t) + e_{i,u}^p, \tag{44}$$

Phase-range $\Phi_{i,u}^{p}(t)$:

$$\Phi_{i,u}^{p}(t) = \gamma_u^p\left(t, t-\tau_u^p\right) + c\left\{\delta t_u(t) - \delta t^p\left(t-\tau_u^p\right)\right\} + \frac{f_1^2}{f_i^2}\delta I_u^p(t) + \delta T_u^p(t) + \lambda_i N_{i,u}^p + \varepsilon_{i,u}^p, \tag{45}$$

where

$\gamma_u^p(t, t-\tau)$: geometric ranges,

$\delta t^p\left(t-\tau_u^p\right)$: satellite delay times,

τ_u^p: radio propagation time,

$\delta t_u(t)$: receiver delay times,

$\delta I_u^p(t)$: ionospheric delay errors,

$\delta T_u^p(t)$: tropospheric delay errors,

$N_{i,u}^p$: integer biases of cycle,

$e_{i,u}^{p}$: pseudorange measurement noise,

$\varepsilon_{i,u}^{p}$: phaserange measurement noise,

c : light speed=299,792,458 [m/s].

The number of frequencies *i* and central frequencies *fi* are shown in Table 4.2-1.

Table 4.2-1 GPS signals: frequencies and wave lengths

L_i band	frequency [MHz]	wavelength [m]
i = 1	f_1 = 1575.42	λ_1 = 0.19
i = 2	f_2 = 1227.60	λ_2 = 0.24
i = 5	f_3 = 1176.45	λ_5 = 0.25

In GNSS techniques, both RTK (Real-Time Kinematic) and PPP (Precise Point Positioning) can be applied to the above observation Eqs. (44) and (45). We introduce the following four GNSS techniques.

(1) RTK GNSS

This technique provides the corrections data in OSR (Observation State Representation) for GNSS precise positioning, that provides the data of the pseudorange $\rho_{i,u}^{p}(t)$ and carrier-phase $\phi_{i,u}^{p}(t)$ at the reference stations to user receivers.

The 3GPP standards have adopted this technique in its specifications of the release 15 [10]. Furthermore, NTT DoCoMo, Softbank Group and the professional distributors provide their services using these techniques as of 2020 in Japan.

(2) Network RTK GNSS

This technique provides the correction data of the pseudorange $\rho_{i,u}^{p}(t)$ and carrier-phase $\phi_{i,u}^{p}(t)$ at non-physical or physical reference stations k', to the user receivers. These corrections are OSRs. Eqs. (44) and (45) mean the SSR data are equivalent to the OSR data, and both representations can be convertible each other.

3GPP standards have adopted this technique in the release 15 [11]. In Japan, several professional distributors provide their services using this technique.

(3) GNSS PPP-AR

The PPP technique provides the satellites clock and orbit corrections, the part of SSRs, to the user receivers. In particular, the PPP-AR (Ambiguity Resolution) technique is relevant to these algorithms. Because the accuracy of the PPP-AR which solves the integer bias of the carrier wave, compare with other 3 techniques.

QZSS provides its PPP service using MADOCA (Multi-GNSS Advanced Demonstrator tool for Orbit and Clock Analysis) to Japan and global area [19].

(4) GNSS PPP-RTK

This technique provides not only the satellite clock and orbit correction, but also the ionospheric and tropospheric corrections to the user receivers.

In Japan, the user receivers can utilize the national PPP-RTK service to use QZSS's CLAS (Centimeter Level Augmentation Service) [14]. During the period from 2011 to 2018, the CMAS (Centimeter-class Augmentation System), the demonstrator of QZSS CLAS, had been utilized in hundreds of application demonstrations [28].

This technique has also applied to 5G (5th Generation) mobile communication networks, new assisted GNSS services [29], and automobile markets [30].

These positioning techniques which are introduced in this chapter, have centimeter-level accuracies. We consider that the detection algorithms in this article can apply these positioning services.

4.3 Hypothesis testing of averaging

A conventional method for detecting a noise-buried displacement is "averaging", which calculates an average of a sample period and compares with a reference. In this section, we conduct a hypothesis testing to check the averaging is significant or not for retrieving the displacement $s_D(t)$ from such measurement data $x(t)$.

On the event that the position μ_0 moves to the other position μ_1, H_0 is the null hypothesis that the displacement have not occurred, and H_1 is the alternate hypothesis that the displacement have occurred. Namely,

$$H_0: \mu_0 = \mu_1, \tag{46}$$

$$H_1: \mu_0 \neq \mu_1. \tag{47}$$

The standard deviation σ of the measurement data $x(t)$ can be constant and known, because a measurement method of GNSS is invariant.

When the long-term average of the position which has not moved is μ, and the average of a sample period is $\bar{X}$ the z-testing value z_i given by

$$z_i = \frac{|\bar{X} - \mu|}{\sqrt{\frac{\sigma^2}{n}}}. \tag{48}$$

where, n is the number of the measurement data.

Fig. 4.3-1 shows an example of actual measurement data $x(t)$ at 1 [Hz] rate for the descriptions of the proposed method. Data A has the displacement of 5[mm] at the time 1201[s] artificially, and Data B does not include the displacement. The measurement data were taken using a receiver of Javad Alpha at the place of35.679°N / 139.147°E, Fuchu, Tokyo on February 22, 2018.

When the displacement does not occur, we obtain μ =− 6.64 [mm] and σ =3.82 [mm] from all period data of Data B. The standard deviation σ has been considered as constant, and it adopts this value. The rejection region is 5%, therefore a z-testing reference z = 1.96 from the characteristics of the Gaussian distribution.

By the way, the measurement period 1 hour comes from the specification of “GNSS static method” in the MLIT authorized manual of the national public surveying. It means an enough period which GNSS observation becomes stable in precise surveying.

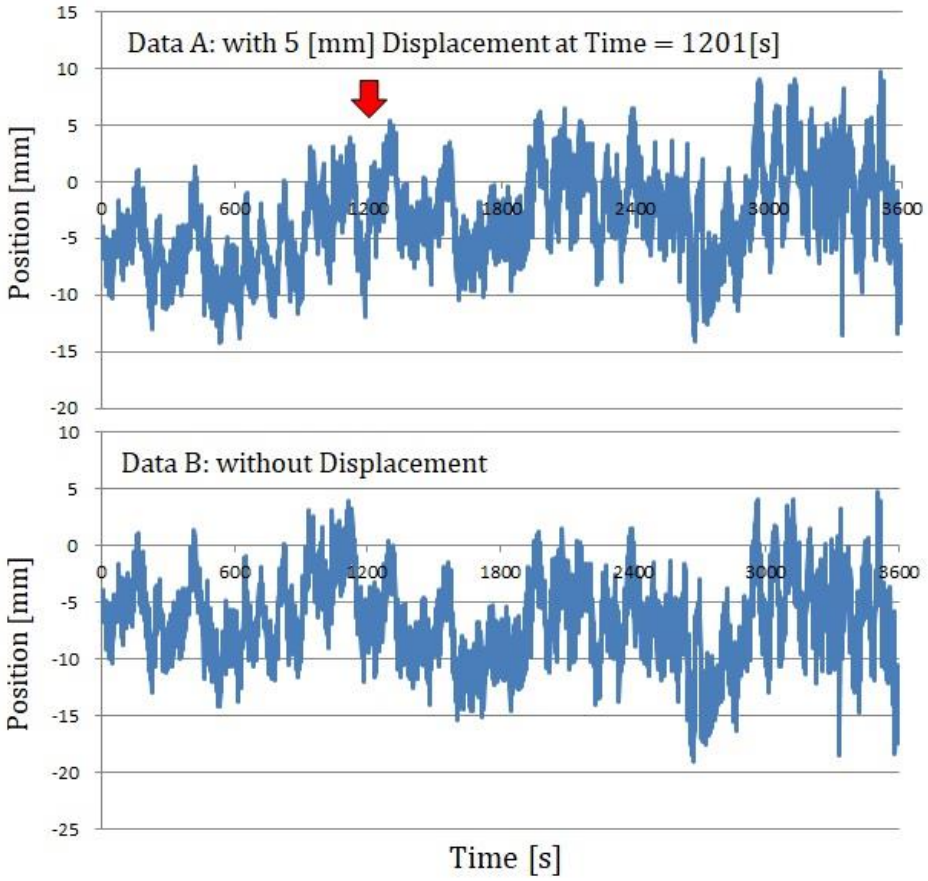

Fig. 4.3-1 Sample measurement data

In case that the displacement exists, we use Data A. The hypothesis testing is conducted in period 1801-2400 [s] after the occurrence time. $\bar{X}_0$ [mm] is an average and z_0 is the z-testing value in this period.

By the way, the sample period 20 minutes comes from the specification of "GNSS shortened static method" and one typical period of GNSS observation.

$$\bar{X}_0 = -8.92 \text{ [mm]}, \tag{49}$$

$$| \bar{X}_0 - \mu | = 2.27 \text{ [mm]}, \tag{50}$$

$$z_0 = 20.58 > z = 1.96. \tag{51}$$

According to the testing result, the null hypothesis has been rejected, and the displacement occurs. But the problem of averaging, which is well-known in the business field, is that "Type I error" which means we judge the displacement exists, easily occurs despite no displacement.

We prove the above fact using Data B with no displacement as follows. In other words, the problem of averaging is to reject null hypothesis H_0, despite there is not displacement, and we check it.

We take 3 sample-periods from t_0[s] to t_1[s] as shown as Table 4.3-1, and test using Eq. (48).

Table 4.3-1 Calculation of z_k

Case	t_0	t_1	$\bar{X}_i$	$\lvert \bar{X}_i - \mu \rvert$	z_i
1	1	1200	-5.69	0.952	8.62
2	1201	2400	-7.27	0.623	5.65
3	2401	3600	-6.83	0.189	1.71

Comparing the reject region 5% and z=1.96, the calculation results of the z-testing value z_i in respective cases are

$$z_1 = 8.62 > \mathrm{z} = 1.96, \tag{52}$$

$$z_2 = 5.65 > \mathrm{z} = 1.96, \tag{53}$$

$$z_3 = 1.72 < \mathrm{z} = 1.96. \tag{54}$$

The null hypothesis has been not always accepted, and some cases must reject it. It means the averaging of conventional method easily makes "Type I error."

We could not adopt the averaging of conventional method for this problem. Therefore, new algorithms must be developed.

4.4 Study for solution

In order to solve this problem, we study the algorithms to use the orthogonal function expansion for GNSS measurement data, which means that

(1) Apply the orthogonal function expansion to the measurement data and represent the sum of components.

(2) Eliminate undesirable components and remain desirable components for our purpose.

(3) Retrieve the occurrence time t_D and the displacement $\Delta\mu$ from the wanted components.

4.4.1 Breakdown by orthogonal functions

At first, we expand the measurement data $x(t)$ to the linear combination of orthogonal functions $\psi_i(t), i = 0, \cdots, n$ such that

$$\Psi(t) = \sum_{i=0}^{n} a_i \psi_i(t)\, dt, \tag{55}$$

where, a_i are the coefficients, $\psi_i(t)$ are the continuous real functions, *n* is the order of the orthogonal functions.

In this thesis, “fit” is used to represent the measurement data as the sum of adequate orthogonal functions. The measurement data $x(t)$ are represented as the vector y such that

$$y \equiv [x(t_0)\ \ x(t_1)\ \ \cdots\ x(t_n)\ ]^{\mathrm{T}}. \tag{56}$$

The coefficient vector a consists of the components a_i, which come from the orthogonal function expansion. It is given by

$$a \equiv [\, a_0 \;\; a_1 \;\; \cdots \;\; a_n \,]^{\mathrm{T}}. \tag{57}$$

Then a matrix $G \in \mathbb{R}^{n \times n}$ is defined using $\psi_i(t)$ such that

$$G \equiv \begin{bmatrix} \psi_0(t_0) & \psi_0(t_1) & \cdots & \psi_0(t_n) \\ \psi_1(t_0) & \psi_1(t_1) & \cdots & \psi_1(t_n) \\ \vdots & \vdots & \ddots & \vdots \\ \psi_n(t_0) & \psi_n(t_1) & \cdots & \psi_n(t_n) \end{bmatrix}. \tag{58}$$

a is solved using the least square method such that

$$a = (G^T G)^{-1} G^{\mathrm{T}} y. \tag{59}$$

We use a in Eq. (59) to eliminate the components of orthogonal functions and calculate the accumulated residual function $R_s(t)$, which is described later. The components are represented as Eq. (55) using the orthogonal functions $\psi_i(t)$.

4.4.2 Identification by elimination

In Eq. (55), a_i and ψ_i come from the characteristics of the original measurement data $x(t)$. In general, the original data are represented the sum of eigenvalues and eigenvectors of themselves. These are inner-data characteristics of $x(t)$.

But it can be said rather difficult to solve from inner-data characteristics of the measurement data. Therefore, we will study the method to mandatorily eliminate specific components by external force and retrieve a noise-buried displacement. In other words, we will eliminate the components which make the displacement invisible.

The residual function is represented as follows. Our algorithms intentionally draw out specific components as Eq. (61).

$$r_s(t) = x(t) - \Psi(t) \tag{60}$$

$$= x(t) - \sum_{i=0}^{n} a_i \psi_i(t)\,. \tag{61}$$

If we can retrieve the step-moved characteristics of the displacement function $s_D(t)$ at the occurrence time t_D, for example, as a clear peak, the occurrence time t_D will be found from the accumulated residual function $R_s(t)$ which is described later.

4.4.3 Role of orthogonal polynomials

In this section, we use the orthogonal "polynomials" as the function $\psi_i(t)$. The orthogonal polynomials are generalized as the Jacobi polynomials, and its special example is the Gegenbauer polynomials.

The Gegenbauer polynomials satisfy the following recursive relation [30].

$$C_0^{\alpha}(t) = 1, \tag{62}$$

$$C_1^{\alpha}(t) = 2\alpha t, \tag{63}$$

$$C_n^{\alpha}(t) = \frac{1}{n}\{c_1 C_{n-1}^{\alpha}(t) - c_2 C_{n-2}^{\alpha}(t)\}, \tag{64}$$

where,

$$c_1 = 2t(n + \alpha - 1), \tag{65}$$

$$c_2 = n + 2\alpha - 2. \tag{66}$$

An easy-to-use case is

$$\alpha = \frac{1}{2}, \tag{67}$$

This formula corresponds to the Legendre polynomials. The respective function is given by

$$P_n(t) = \frac{1}{2^n}\sum_{i=0}^{n}\binom{n}{i}^2 (t-1)^{n-i}(t+1)^i. \tag{68}$$

In this article, we use the Legendre polynomials as one of the Gegenbauer polynomials as a set of orthogonal functions.

The components of orthogonal polynomials do not simply correspond to frequency components as the trigonometric functions. The 0th and 1st order components are a constant and linear function with respect to time. These components have clear physical meanings and are well-used in various analysis works.

We clarify the merit of the orthogonal polynomials in the following paragraphs. These algorithms can find a clear peak at the occurrence time of displacement using 0th and 1st order components of the orthogonal polynomials.

The 0th and 1st order components of the Legendre polynomials are

$$P_0(t) = 1, \tag{69}$$

$$P_1(t) = t. \tag{70}$$

Therefore,

$$P(t) = a_0 P_0(t) + a_1 P_1(t) \tag{71}$$

$$= a_0 + a_1 t. \tag{72}$$

Here, we put $\mu_0 = 0$ and fit $P(t)$ to the displacement function $s_D(t)$. The coefficients are given by

$$a_0 = -\frac{\Delta\mu}{4}, \tag{73}$$

$$a_1 = \frac{3\Delta\mu}{2T}. \tag{74}$$

Then the residual function $r_s(t)$ is derived from the displacement function $s_D(t)$ such that

$$r_s(t) = s_D(t) - P(t). \tag{75}$$

Dividing cases before and after the time t_D[s],

$$r_s(t) = \begin{cases} \dfrac{\Delta\mu}{4} - \dfrac{3\Delta\mu}{2T} t & (t < t_D), \\ \dfrac{5\Delta\mu}{4} - \dfrac{3\Delta\mu}{2T} t & (t \geq t_D). \end{cases} \tag{76}$$

Furthermore, we integrate the residual function $r_s(t)$ with respect to time t and obtain the accumulated residual functions $R_s(t)$ such that

$$R_s(t) = \int_0^t r_s(\tau)\, d\tau. \tag{77}$$

Here, we divide the cases before and after the occurrence time t_D such that

In period $t < t_D$:

$$R_s(t) = \int_0^t \left(\frac{\Delta\mu}{4} - \frac{3\,\Delta\mu}{2\,T}\tau\right) d\tau \tag{78}$$

$$= \frac{\Delta\mu}{4}t - \frac{3\,\Delta\mu}{4\,T}t^2. \tag{79}$$

In period $t \geq t_D$:

$$R_s(t) = R_D + \int_{t_D}^t \left(\frac{5\,\Delta\mu}{4} - \frac{3\,\Delta\mu}{2T}\tau\right) d\tau \tag{80}$$

$$= R_D + \frac{5\,\Delta\mu}{4}(t - t_D) - \frac{3\,\Delta\mu}{4\,T}(t^2 - t_D^2), \tag{81}$$

where,

$$R_D = R_s(t_D) = \lim_{u \to t_D} \int_0^u r_s(\tau)\, d\tau$$

$$= \lim_{u \to t_D} \int_0^u \left(\frac{\Delta\mu}{4} - \frac{3\,\Delta\mu}{2\,T}\tau\right) d\tau$$

$$= \lim_{u \to t_D} \left[\frac{\Delta\mu}{4}\tau - \frac{3\,\Delta\mu}{2\,T}\tau^2\right]_0^u$$

$$= \frac{\Delta\mu\, t_D}{4}\left(1 - \frac{3}{T}t_D\right). \tag{82}$$

Fig. 4.4-1 shows an actual example of this calculation. In this case, the parameters are $\Delta\mu$=5 [mm], T=60 [s] and t_D=30 [s].

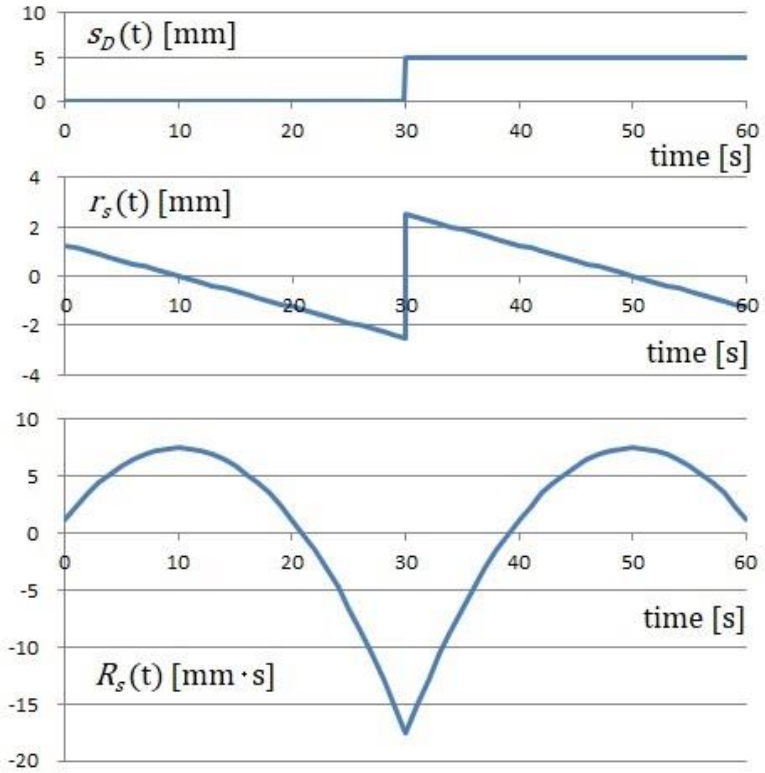

Fig. 4.4-1 Deviation of a clear peak

In Fig. 4.4-1, we show that the accumulated residual function $R_s(t)$ can retrieve the occurrence time t_D[s] as a clear peak. Therefore, we can utilize it for finding the occurrence time.

In reality, the above algorithms are applied to noise-buried measurement data. The algorithms have a great merit to detect the candidates of the occurrence time. This discussion reveals the effect of the 0th and 1st order components of the orthogonal polynomials.

In addition, we must consider the role of higher order components than 1st order of the orthogonal polynomials. Such higher order components represent higher power spectrum components. But these components of the Legendre polynomials are different from the Fourier series. It means higher order components of polynomials do not correspond perfect frequency components. Therefore, we can obtain only candidates of the true occurrence time, and it has become the first step, not a final solution.

Fig. 4.4-2 shows an actual example of the accumulated residual function $R_s(t)$. There are several peaks. They can be examples of the candidates t_c of the true occurrence time t_D.

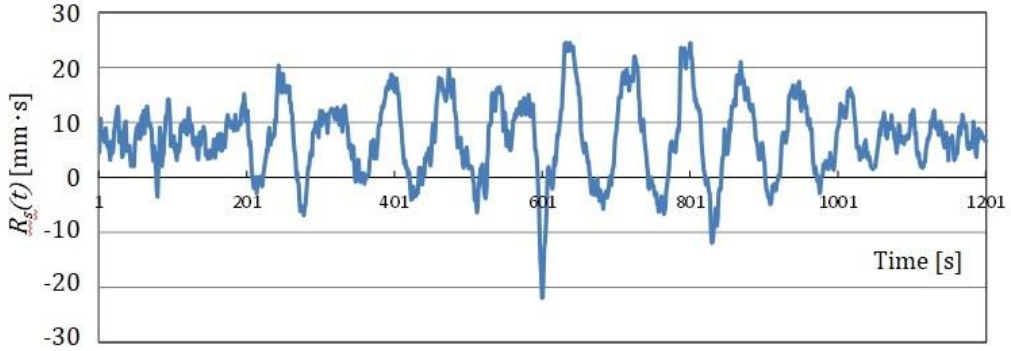

Fig. 4.4-2 Example of the accumulated residual function

The above study clarifies that we can obtain the candidates of the occurrence time using the Legendre polynomials. If obtaining the candidates t_c of the occurrence time and eliminating unwanted components, we can identify the occurrence time. This is the next step, and it will be discussed in Sec. 4.5.

4.4.4 Considering Fourier series

In this subsection, we discuss about the use of the Fourier functions. Orthogonal functions are the sum of the 0th and higher order components, and represented by

$$F(t) = \psi_0(t) + \sum_{n=1}^{N} \psi_n(t)\,, \tag{83}$$

The orthogonal functions are given by

$$\psi_0(t) = \frac{a_0}{2}, \tag{84}$$

$$\psi_n(t) = a_n \cos\frac{2\pi nt}{T} + b_n \sin\frac{2\pi nt}{T}. \tag{85}$$

where, T is the measurement period, and

$$a_n = \frac{2}{T}\int_0^T x(t)\cos\frac{2\pi nt}{T}\,dt, \tag{86}$$

$$b_n = \frac{2}{T}\int_0^T x(t)\sin\frac{2\pi nt}{T}\,dt. \tag{87}$$

There are difficulties in the algorithms using the Fourier series. The displacement function $s_D(t)$ and the observation noise $w(t)$ have conspired their power spectrums in the band which is close to the sampling interval 1 [Hz], the upper limit of observation. Therefore, it is difficult to distinguish them using the Fourier series.

Furthermore, there is another difficulty. The Fourier series automatically coordinate the phase against our intention. This effect deletes the evidence of the occurrence time t_D by the landslide. It means that we lost the most wanted information for this problem.

According the above two reasons, the Fourier functions are ill-adapted to the problem.

4.5 Determining the occurrence time

We have obtained the candidate t_c of the occurrence time in Sec. 4.4. All we should do is to clarify how to determine true or not and find the occurrence time t_D.

In order to solve the above problem, we re-write a displacement model such as Fig. 4.5-1 for the 2nd step of the algorithms,

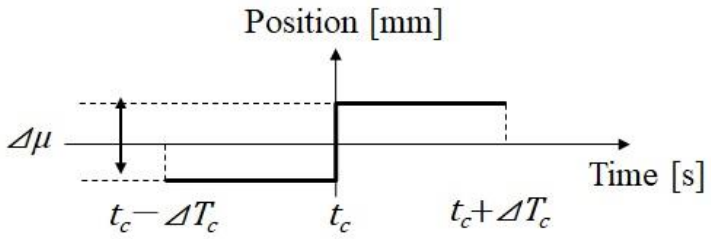

Table 4.5-1 Displacement model in 2nd step

where t_c is the candidate of the true occurrence time t_D. Namely if t_c is true, t_c=t_D.

The measurement data $x(t - t_D)$ can be divided into the even function $x_e(t - t_D)$ and the odd function $x_o(t - t_D)$ on the time t_D such that

$$x(t - t_D) = x_e(t - t_D) + x_o(t - t_D), \tag{88}$$

where $x_e(t - t_D)$ and $x_o(t - t_D)$ behave as

$$x_e(-t - t_D) = x_e(t - t_D), \tag{89}$$

$$x_o(-t - t_D) = -x_o(t - t_D). \tag{90}$$

$x_e(t - t_D)$ and $x_o(t - t_D)$ are orthogonal each other such that

$$\int_{t_D-\Delta T}^{t_D+\Delta T} x_e(t - t_D)x_o(t - t_D)dt = 0\,. \tag{91}$$

We can consider that the displacement function $s_D(t)$ is just the odd function, if we put the occurrence time t_D at the origin. Because this displacement is an irreversible phenomenon, and all landslides are irreversible. Therefore, we can say they are the odd functions.

This fact represents the characteristics of the displacement function $s_D(t)$. It becomes an odd function on the occurrence time t_D shown as

$$s_D(-t) - \frac{\mu}{2} = -s_D(-t) - \frac{\mu}{2}. \tag{92}$$

In other words, $s_D(t)$ never have the even components primitively. Therefore, if we eliminate the even components, it is able to obtain the information of the displacement $s_D(t)$. From these discussions, we will precisely eliminate unwanted components using the orthogonal even functions $E(t - t_c)$, which have the following characteristic, and remain components of $s_D(t)$ only.

$$E(-t - t_c) = E(t - t_c). \tag{93}$$

We calculate using actual data, and use the measurement data, which are artificially added a step of 5[mm] to PPP-RTK data utilizing QZSS CLAS, mentioned in Subsec. 4.2.3.

On the stage obtaining the candidates t_c, we eliminate 0th and 1st components of the Legendre functions, similarly to Sec. 4.4.3.

We use the cosine functions, to eliminate the unwanted even components for determining the true occurrence time. The cosine functions are used as the orthogonal even functions $E(t - t_c)$ for eliminate the observation noise $w(t)$.

$$E(t - t_c) = \sum_{n=0}^{N} a_n \cos \frac{2\pi(n+1)(t - t_c)}{T}. \tag{94}$$

In this case, the order must cover the frequency band, which covers the disturbance of ionospheric delay. In general, the ionospheric disturbance has the variance of approximately 1 minute. Therefore, we take the order which covers this disturbance. The numerical example is 35th order in maximum.

We integrate a residual function, which eliminates the orthogonal functions, and calculate the accumulated residual function. This result is shown as Fig. 4.5-2. It shows a clear peak when the candidate is true.

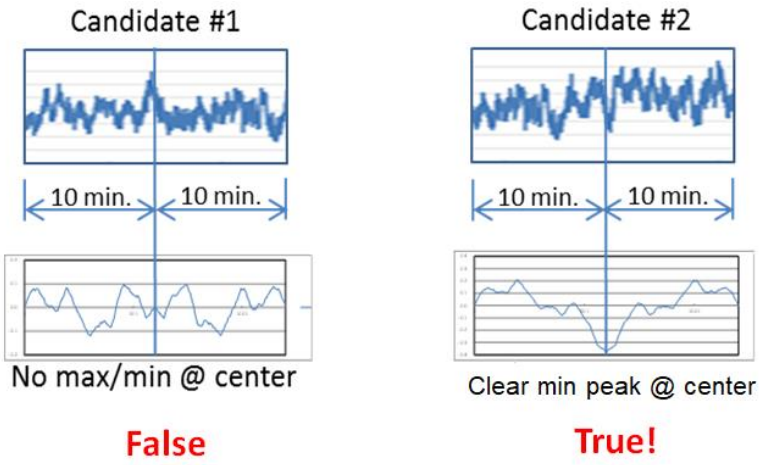

Table 4.5-2 Clear peak appearance in a true case only

According to this result, if the candidate is false, we cannot find the clear peak. On the other hand, if the candidate is true, we can find the clear peak. Therefore, it is able to determine true or not of a candidate t_c. After determining the occurrence time t_c, we can calculate the length of the displacement $\Delta\mu$ by taking an average difference before and after the occurrence time t_D.

The study of this section has clarified that we can determine the candidate is true or not, using the elimination of the observation noise $w(t)$ from the measurement data $x(t)$ with the candidates t_c of the occurrence time t_D.

These algorithms are to fit the even functions and eliminate the unwanted noise $w(t)$ from the original data $x(t)$. By using this method, we can determine the true occurrence time t_D and retrieve the millimeter-scale displacement $\Delta\mu$.

4.6 Integration of algorithms

We can derive a new and practical solution by integrating the algorithms described in the previous sections. The algorithms consist of two steps. The 1st step is to find the candidates t_c of the occurrence time t_D. The 2nd step is, using the result of the 1st step, to determine the occurrence time t_D and displacement $\Delta\mu$. In actuality, the processing runs on the discrete time t_k. We summarize 2-step algorithms in the following sections.

This method can reduce the displacement measurement time from the current 24 [h] to approximately 1 [h] in quasi-real time to promptly warn of impeding landslide disasters.

4.6.1 Candidate of the occurrence time

The 1st step is the following procedure to find a candidate of the occurrence time t_c.

1) Take the measurement data $x(t_k)$ during the time period T on the discrete time t_k with interval ΔT for digital measurement and processing. For example, T =3600[s].

$$x(t_k) : 1 \leq t_k < T. \tag{95}$$

2) Fit and solute the coefficient a_n of the Legendre polynomials to the measurement data $x(t_k)$. For example, N=35.

$$P(t_k) = \sum_{n=0}^{N} a_n P_n(t_k)\,, \tag{96}$$

where,

$$P_n(t_k) = \frac{1}{2^n}\sum_{i=0}^{N} \binom{n}{i}^2 (t_k - 1)^{n-i}(t_k + 1)^i. \tag{97}$$

3) Eliminate the components of Eq. (96) from the original measurement data $x(t_k)$.

$$r_s(t_k) = x(t_k) - P(t_k). \tag{98}$$

4) Integrate the residual function $r_s(t_k)$ from the start time 0 to t_k and obtain the accumulated residual function $R_s(t_k)$. The integration is numerically executed using the Simpson's rule for example.

$$R_s(t_k) = \int_0^{t_k} r_s(\tau)\, d\tau. \tag{99}$$

5) We can find a number of clear peaks and make them the candidate t_c of the occurrence time.

4.6.2 Occurrence time and displacement

The 2nd step is the following procedure to find the occurrence time and displacement t_D and the displacement $\Delta\mu$.

1) Take the measurement data $x'(t_k)$ during $t_c - \Delta t_c$ to $t_c + \Delta t_c$ on the re-defined discrete time t_k with interval ΔT for digital measurement and processing. For example, Δt_c=600 [s].

$$x'(t_k) : t_c - \Delta t_c \le t_k < t_c + \Delta t_c. \tag{100}$$

2) Eliminate 0th and 1st terms of the Legendre polynomials.

$$x''(t_k) = x'(t_k) - \{a_0 P_0(t_k) + a_1 P_1(t_k)\}. \tag{101}$$

3) Fit the cosine function to $x''(t_k)$, and eliminate the lower order components, and obtain the residual function $r_{s\prime}(t_k)$. For example, $N = 35$.

$$r_{s\prime}(t_k) = x''(t_k) - \sum_{n=0}^{N} a_n \cos\frac{2\pi(n+1)t_k}{2\Delta T_c}. \tag{102}$$

4) Integrate $r_{s\prime}(t_k)$ from $t_c - \Delta t_c$ to t_k and obtain the accumulated residual function $R_{s\prime}(t_k)$. The integration is numerically executed using the Simpson's rule for example.

$$R_{s\prime}(t_k) = \int_{t_c - \Delta t_c}^{t_k} r_{s\prime}(\tau)\, d\tau. \tag{103}$$

5) Check $R_{s\prime}(t_k)$, and find the clear peaks at the candidate t_c. If so, t_c is the true value t_D. If not a clear peak, reject the candidate t_c.

6) Take the average of $x(t_k)$ before and after t_D respectively, and calculate the difference, and obtain the displacement $\Delta\mu$.

5 EXPERIMENTS FOR MILLIMETER DISPLACEMENT DETECTION

5.1 Experiments of occurrence

In this chapter, we show numerical examples of experiments. These experiments were conducted in Tokyo area of Japan, As GNSS technique, we used RTK mentioned in Subsec. 4.2.3 for checking the algorithms. Our equipment made an artificial input of displacement and measured this displacement using the proposed algorithms in this thesis.

5.1.1 Experiment 1

In Table 5.1-1, we show the conditions of this experiment. Fig. 5.1-1 shows detected clear peaks at the occurrence time. The horizontal axis is an elapsed time from the start time. Table 5.1-1 shows the result of these displacement measured values, where the columns of UTC present the starting time of the experiment in Coordinated Universal Time. The displacement was given at 600 [s] later from the start time.

Table 5.1-1 Condition of Experiment 1

No.	Item	Description
1	Place	35.679°N / 139.147°E
2	Date	February 22, 2018
3	Equipment	Javad Alpha
4	Direction	Easting
5	Input	7.5 mm

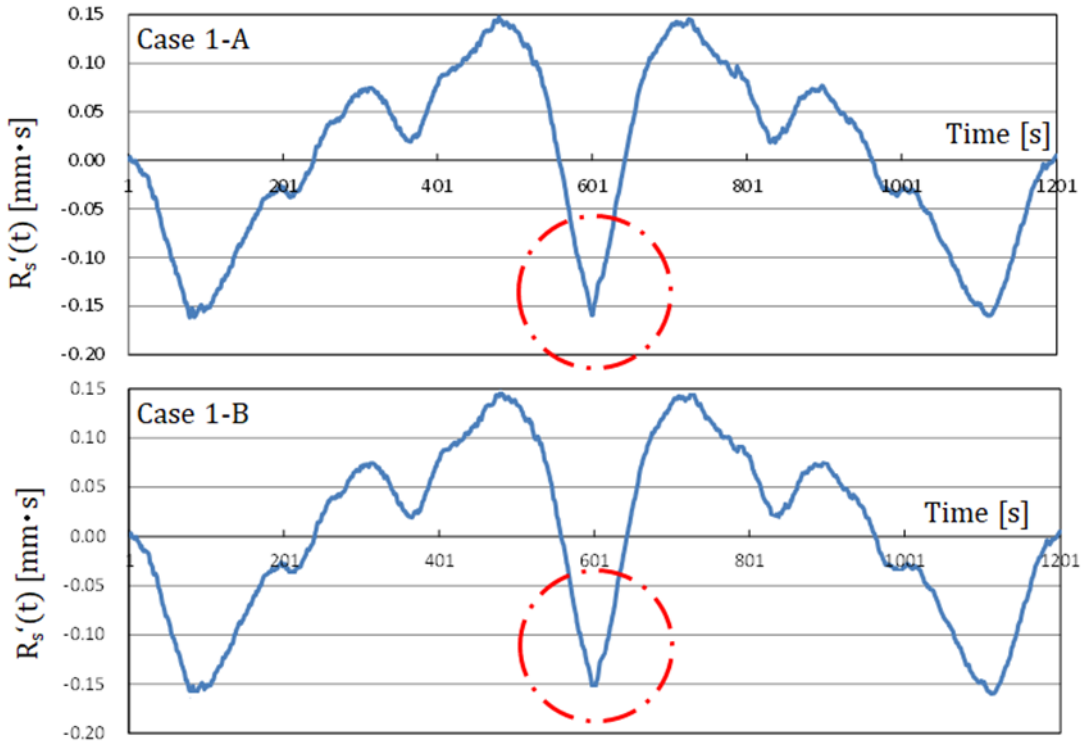

Fig. 5.1-1 Detection of the occurrence time in Experiment 1

Table 5.1-2 Results of Experiment 1

Case	UTC	True value	Estimated value
1-A	00:00	7.5 mm	8.5 mm
1-B	06:00	7.5 mm	5.8 mm

The measured values could be detected closer displacement to the true value in both cases. Such measured values have been enough accurate that an administrator of the infrastructures release a warning to citizens in actual services.

5.1.2 Experiment 2

In Table 5.1-3, we show the conditions of this experiment.

Table 5.1-3 Condition of Experiment 2

No.	Item	Description
1	Place	35.679°N / 139.147°E
2	Date	February 22, 2018
3	Equipment	Javad Alpha
4	Direction	Easting
5	Input	5 mm

Fig. 5.1-2 shows detected clear peaks at the occurrence time. Table 5.1-4 shows the result of these displacement measured values.

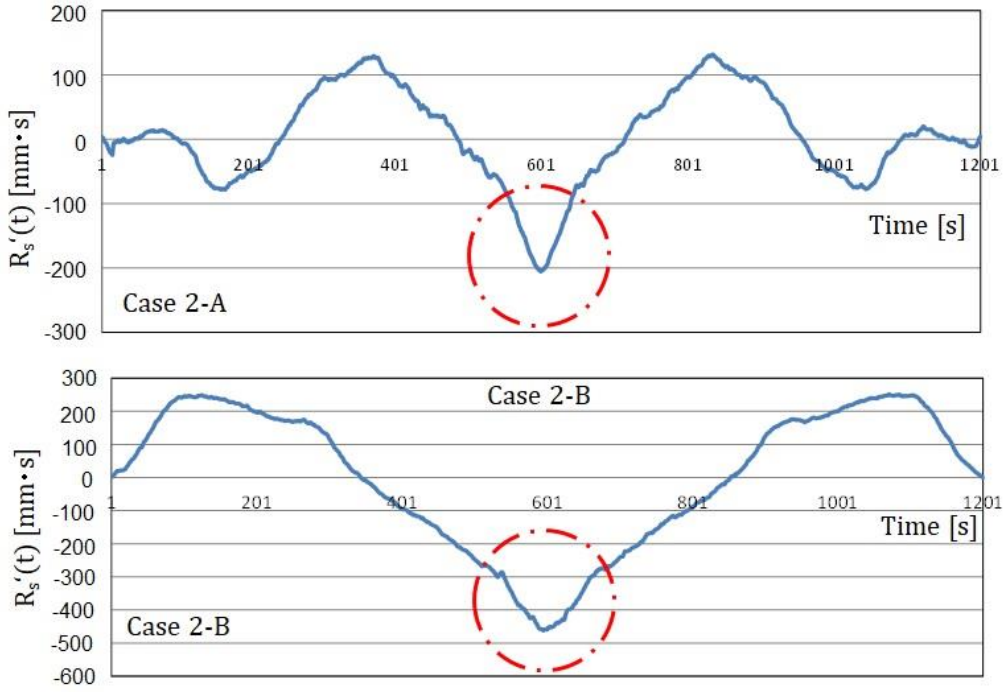

Fig. 5.1-2 Detection of the occurrence time in Experiment 2

Table 5.1-4 Results of Experiment 2

Case	UTC	True value	Estimated value
2-A	00:20	5.0 mm	4.7 mm
2-B	06:20	5.0 mm	7.5 mm

The measured values could be detected closer displacement to the true value in all of the cases. Such measured values have been enough accurate that an administrator of the infrastructures release a warning to citizens in actual services.

5.1.3 Experiment 3

In Table 5.1-5, we show the conditions of this experiment. Fig. 5.1-3 shows detected clear peaks at the occurrence time. Table 5.1-6 shows the result of these displacement measured values.

Table 5.1-5 Condition of Experiment 2

No.	Item	Description
1	Place	35.679°N / 139.147°E
2	Date	February 22, 2018
3	Equipment	Javad Alpha
4	Direction	Easting
5	Input	2.5 mm

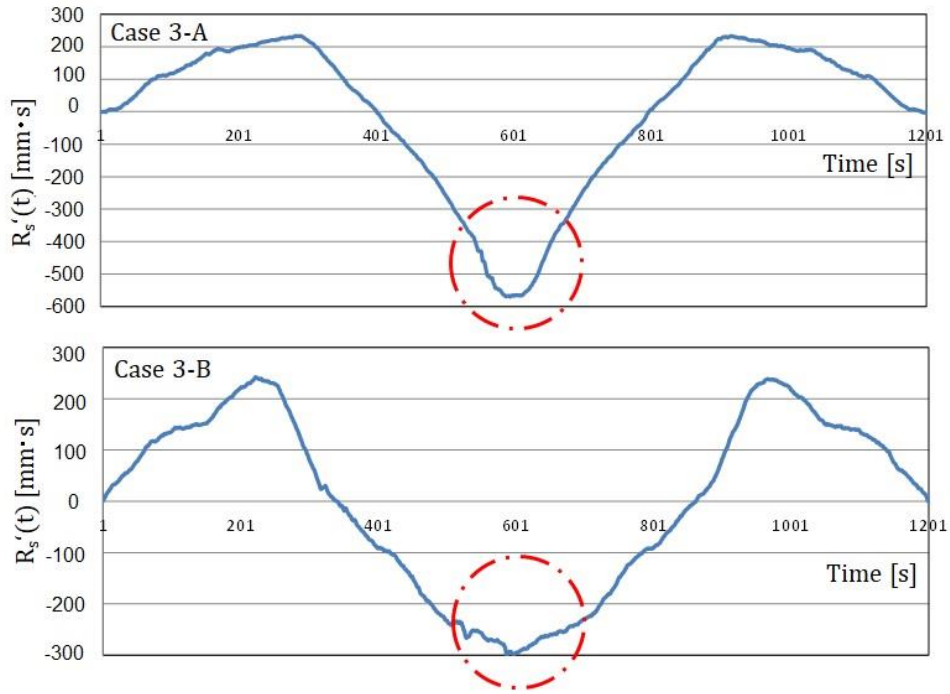

Fig. 5.1-3 Detection of the occurrence time in Experiment 3

Table 5.1-6 Results of Experiment 2

Case	UTC	True value	Measured value
3-A	00:40	2.5 mm	3.8 mm
3-B	06:40	2.5 mm	3.2 mm

The measured values could be detected closer displacement to the true value in all of the cases. Such measured values have been enough accurate that an administrator of the infrastructures release a warning to citizens in actual services.

There are other techniques of GNSS precise positioning which are described in Subsec. 4.2.3. Application of this algorithms to these techniques are our future works.

5.2 Summary for Millimeter Detection

In this thesis, the author addressed the mathematical algorithms to measure a destructive displacement buried in noise using GNSS precise positioning and the orthogonal function expansion of its positioning result. This method can reduce the displacement measurement time from the current 24 [h] to approximately 1 [h] in quasi-real time to promptly warn of impeding landslide disasters.

The major application is the detection of a landslide which is one of most intimidating disasters. In reality, there are 525 thousand points as sediment disaster dangerous places in Japan.

This mathematical algorithm to retrieve millimeter-scale displacement in observation noise of GNSS precise positioning. Principally speaking, these algorithms can be applied to onto RTK, PPP, and GNSS precise positioning in not only Japan but also other regions. This method will inform the foreboding of a destructive landslide and will save many lives and infinite property of assets in catastrophic disasters [19,20].

6 CONCLUSIONS

In this thesis, novel high-accuracy positioning methods of Global Navigation Satellite System (GNSS) were proposed for centimeter augmentation and millimeter displacement detection, and its accuracy and convergence performances were validated.

Firstly, the author designed the centimeter-accurate positioning assistance system for realtime navigation and positioning using the 5G mobile communication service. In the comparison to the existing system using the QZSS satellite, this design made the horizontal accuracy from 3 [cm] to approximately 1 [cm] and makes the convergence time from 60 [s] to 3 [s]. These are the highest performances as the unidirectional assistance of real-time GNSS positioning which should be implemented into the smart cities which are developed today.

Secondly, the author also developed millimeter-accurate displacement detection in semi-realtime. The thesis discussed mathematical algorithms to measure a destructive displacement buried in noise using GNSS precise positioning and the orthogonal function expansion of its positioning result. The algorithm must retrieve a millimeter-scale displacement in observation noise; therefore, they apply the orthogonal functions from the class of Gegenbauger polynomials and the orthogonal even functions. This method can reduce the displacement measurement time from the current 24 [h] to approximately 1 [h] in quasi-real time to promptly warn of impeding landslide disasters. Thus, the proposed method can save many lives and considerable property.

Thus, a realtime centimeter augmentation and semi-realtime millimeter displacement detection method with high-accuracy and short observation span can be obtained proposed by using GNSS systems and the proposed method. The proposed method can be a fundamental technology that can enable automated navigation and high-accuracy positioning, safe and manageable spatial migration and disaster management, and improvement of the quality of life.

REFERENCES

[1] Satellite Positioning Research and Application Center, *Centimeter-class Augmentation System: Report of Third-party Assessment*, in Japanese, SPAC (2013)

[2] U.S. Space and Missile Systems Center, *NAVSTER GPS Space Segment/Navigation User Interface,* IS-GPS-200M (2021)

[3] Cabinet Office of Japan: *Quasi-Zenith Satellite System Performance Standard,* PS-QZSS-001 (2018)

[4] GLONASS Navigation Satellite System, *GLONASS Interface Control Document Navigational Radiosignal In Bands L1, L2, Edition 5.1* (2008)

[5] Galileo Navigation Solutions, *European GNSS (Galileo) Open Service Signal In Space Interface Control Document (OS SIS ICD), Issue 2.0* (2021)

[6] China Satellite Navigation Office, *BeiDou Navigation Satellite System, Open Service Performance Standard, Version 2.0* (2018)

[7] ISRO, *IRNSS Signal In Space ICD for Standard Positioning Service, Ver. 1.1* , ISRO-IRNSS-ICD-SPS (2017)

[8] European Commission and GSA: GNSS Market Report Issue 5, p. 10 (2017), https://www.gsa.europa.eu/market/gnss-market

[9] Y. Gao and X. Shen: A New Method for Carrier-Phase-Based Precise Point Positioning, *Journal of The Institute of Navigation*, Vol. 49, No. 2 (2002)

[10] G. Wübbena, A. Bagge and M. Schmitz: Network-Based Techniques for RTK Applications, *GPS JIN 2001, GPS Society, Japan Institute of Navigation,* November 14-16, Tokyo, Japan (2001)

[11] G. Wübbena, A. Bagge and M. Schmitz: PPP-RTK: Precise Point Positioning using State Space Representation in Real-Time Networks, *Proceedings of the 18th International Technical Meeting of the Satellite Division of the Institute of Navigation (ION GNSS 2005)*, pp. 2584-2594, Long Beach, CA, U.S.A. (2005)

[12] K. Asari, Y. Kubo and S. Sugimoto: Design of GNSS PPP-RTK Assistance System and its Algorithms for 5G Mobile Networks, *Transactions of the Institute of Systems, Control and Information Engineers,* Vol.33, No. 1, pp. 31-37 (2020)

[13] Y. Sato, M. Miya, S. Fujita and R. Hirokawa: Selective Augmentation of Positioning Satellites in Centimeter Level Augmentation Service, *IPNTJ Journal,* Vol.7, No. 2, pp. 11-20 (2016)

[14] Cabinet Office of Japan: Quasi-Zenith Satellite System Interface Specification, Centimeter Level Augmentation Service, IS-QZSS-L6-001 (2018)

[15] 3rd Generation Partnership Project: *3GPP specification release 8,15 and 16* (2019)

[16] Radio Technical Committee for Maritime Service (RTCM) : Differential GNSS (Global Navigation Satellite Systems) Services - Version 3, *RTCM Standard 10403.3* (2016)

[17] J. Saastamoinen: Contribution to the theory of atmosphere refraction, parts 1-3, Bulletin of Geodesique, (105, 106, 107), pp. 279-298, pp. 383-397, pp. 13-34 (1973)

[18] A. E. Niell: Global mapping functions for the atmosphere delay at radio wavelengths, Journal of Geophysical Research, Vol. 101, No. B2, pp. 3227-3246 (1996)

[19] T. Katayama: *Applied Kalman Filters, 2nd edition,* in Japanese, Asakura-Shoten, Tokyo (2000)

[20] Japan Ministry of Land, Infrastructure, Transport and Tourism (MLIT): Sediment disaster danger places by prefectures, https://www.mlit.go.jp/common/001286018.pdf, Retrieved on 2020-07-25. (in Japanese)

[21] Japan Ministry of Land, Infrastructure, Transport and Tourism (MLIT), Kinki Regional Development Bureau: Landslide Video on National Highway Route 168 in Yoshino-gun, Nara Prefecture, https://www.kkr.mlit.go.jp/bousai/taiou/kinki/h23/jisuberi-0810/index.html, Retrieved on 2020-02-01.

[22] I. Mikami, K. Asari and M. Saito: New Method to Retrieve Millimeter Class Displacement from RTK/PPP-RTK Measurement Data, *Proceedings The 16th IAIN World Congress 2018*, B7-2, Makuhari Messe, Japan (2018)

[23] I. Mikami, M. Saito and K. Asari: Detection Method of mm-class Step Displacement using GNSS Positioning Result with cm-class Accuracy, *2018 IPNTJ National Convention*, 20, Tokyo University of Marine Science and Technology, Japan (2018) (in Japanese)

[24] Shamen-net Study Group: Shamen-net kenkyu-kai (the study group for slope displacement measurement), http://www.shamen-net.org/detail/012.html, Retrieved on 2020-11-01. (in Japanese)

[25] H. L. Van Trees, K. L. Bell and Z. Tian: Detection, Estimation, and Modulation Theory, Part I - Detection, Estimation, and Filtering Theory, Second Edition, *Wiley (*2013)

[26] Y. Kubo: Applications of the Kalman Filter to Satellite Navigation Systems, in Japanese, *Journal of ISCIE,* Vol. 64, No. 1, pp. 33-38 (2020)

[27] JAXA: MADOCA Real-Time Products, https://ssl.tksc.jaxa.jp/madoca/public/public_index_en.html, Retrieved on 2020-02-01.

[28] M. Saito, Y. Sato, M. Miya, M. Shima, Y. Omura, J. Takiguchi and K. Asari: Centimeter-class Augmentation System Utilizing Quasi-Zenith Satellite, *Proceedings of the 24th International Technical Meeting of the Satellite Division of the Institute of Navigation (ION GNSS 2011)*, pp.1243-1253, Portland, OR, U.S.A. (2011)

[29] K. Asari, Y. Kubo and S. Sugimoto: Design of GNSS PPP-RTK Assistance System and its Algorithms for 5G Mobile Networks, *Transaction of ISCIE, Systems, Control, and Information*, Vol.33, No.1, pp. 31-37 (2020)

[30] S. Vana, J. Aggrey, S. Bisnath, R. Leandro, L. Urquhart and P. Gonzalez: Analysis of GNSS Correction Data Standards for the Automotive Market, *Proceedings of the 31st International Technical Meeting of the Satellite Division of The Institute of Navigation (ION GNSS+ 2018)*, pp.4197-4214, Miami, FL, U.S.A. (2018)

[31] S. Iyanaga and Y. Kawada: Gegenbauer Polynomials (Gegenbauer Functions), *Appendix A, Table 20.I in Encyclopedic Dictionary of Mathematics*, pp. 1477-1478, MIT Press (1980)

[32] S. Sugimoto and R. Shibazaki (Eds.): GPS Handbook, in Japanese, Asakura-shoten (2010)

[33] S. Sugimoto and Y. Kubo: GNSS regressive models and precise point positioning: *Proc. 36 th ISCIE International Symposium on Stochastic Systems Theory and its Applications*, pp. 159-164 (2004)

[34] Y. Kubo, S. Fujita and S. Sugimoto: Estimation and validation of integer ambiguity in carrier phase GPS positioning; *International Journal of Innovative Computing, Information & Control*, Vol. 4, No. 1, pp. 205-210 (2000)

[35] Y. Kubo, H. Tanaka, M. Ohashi and S. Sugimoto: Long baseline GNSS relative positioning with estimating ionospheric and tropospheric delays and their gradients: *Proc. of the 12th ISCIE Int. Symp. on Stochastic Systems Theory and Its Applications (SSS 2010)*, pp. 228-235 (2010)

[36] P. Misra and P. Enge: *Global Positioning System; Signals, Measurements, and Performance (Revised Second Edition)* , Ganga-Jamuna Press (2010)

[37] B.W. Parkinson and J. J. Spilker Jr. (Eds.): *Global Positioning System: Theory and Applications*, Vol 1, II, AIAA (1997)

[38] P. Teunissen and O. Montentruck (Eds.): Springer Handbook of Global Navigation Satellite Systems, 1st edition, Springer (2017)

[39] F. van Diggelen, Y. J. Morton, J. J. Spilker Jr., B. W. Parkinson, S. Lo and G. Gao (Eds.): Position, Navigation, and Timing Technologies in the 21st Century: Integrated Satellite Navigation, Sensor Systems, and Civil Applications, Wiley-IEEE Press (2021)

[40] J. W. Betz: Engineering Satellite-Based Navigation and Timing: Global Navigation Satellite Systems, Signals, and Receivers, Wiley-IEEE Press (2015)

[41] S. Pace, Gerald Frost, D. R. Frelinger, D. Fossum, I. Lachow, D. Wassem and M. M. Pinto: *The Global Positioning System: Assessing National Policies*, RAND Corporation (1995)

[42] M. Ohashi, T. Hattori, Y. Kubo and Sugimoto: Multi-Layer Ionospheric VTEC Estimation for GNSS Positioning, *Proceedings of the 43rd ISCIE International Symposium on Stochastic Systems Theory and Its Applications*, pp. 251-257, Oct. 29-29 (2011)